Title

Inputs to the locus coeruleus from the periaqueductal gray and rostroventral medulla shape opioid-mediated descending pain modulation

Journal

Science Advances, 10(17)

ISSN

2375-2548

Authors

Lubejko, Susan T

Livrizzi, Giulia

Buczynski, Stanley A

et al.

Publication Date

2024-04-26

DOI

10.1126/sciadv.adj9581

NEUROSCIENCE

Inputs to the locus coeruleus from the periaqueductal gray and rostroventral medulla shape opioid-mediated descending pain modulation

Susan T. Lubejko[1,2], Giulia Livrizzi[1,3], Stanley A. Buczynski[1,4], Janki Patel[1], Jean C. Yung[1], Tony L. Yaksh[5], Matthew R. Banghart[1]*

The supraspinal descending pain modulatory system (DPMS) shapes pain perception via monoaminergic modulation of sensory information in the spinal cord. However, the role and synaptic mechanisms of descending noradrenergic signaling remain unclear. Here, we establish that noradrenergic neurons of the locus coeruleus (LC) are essential for supraspinal opioid antinociception. While much previous work has emphasized the role of descending serotonergic pathways, we find that opioid antinociception is primarily driven by excitatory output from the ventrolateral periaqueductal gray (vlPAG) to the LC. Furthermore, we identify a previously unknown opioid-sensitive inhibitory input from the rostroventromedial medulla (RVM), the suppression of which disinhibits LC neurons to drive spinal noradrenergic antinociception. We describe pain-related activity throughout this circuit and report the presence of prominent bifurcating outputs from the vlPAG to the LC and the RVM. Our findings substantially revise current models of the DPMS and establish a supraspinal antinociceptive pathway that may contribute to multiple forms of descending pain modulation.

INTRODUCTION

The midbrain and brainstem descending pain modulatory system (DPMS) alters spinal outflow of ascending nociceptive signals. Current models of the DPMS emphasize excitatory projections from ventrolateral periaqueductal gray (vlPAG) to the rostroventromedial medulla (RVM), which sends projections to the spinal cord dorsal horn that bidirectionally modulate incoming noxious sensory information through serotonergic and opioidergic mechanisms (*1*, *2*). Endogenous and exogenous opioids are thought to produce analgesia via disinhibition of vlPAG→RVM projection neurons (*3*–*5*). The RVM and, to some extent, the PAG are composed of On-, Off-, and neutral cells, which are defined electrophysiologically by their activity preceding a nocifensive response (*6*–*8*).

In addition to serotonin, intrathecal pharmacological studies in rodents implicate spinal noradrenaline (NA) signaling in descending pain modulation, whether triggered by electrical or pharmacological stimulation of the vlPAG, systemic morphine, or local opioid administration within the vlPAG (*9*–*14*). Spinal serotonin can both suppress and facilitate nociceptive processing and pain behaviors (*15*–*17*), whereas spinal NA is more consistently reported as antinociceptive and inhibiting dorsal horn nociceptive processing. Previous work implicates midbrain and brainstem catecholaminergic cell groups as the likely sources of spinal NA, especially the locus coeruleus (LC), also known as the A6 nucleus, which sends both ascending projections from dorsal LC to supraspinal areas and descending projections from ventral LC to the spinal cord (*18*–*25*). Stimulation of ventral LC in rats causes antinociception that depends on spinal NA, while stimulation of dorsal LC is pronociceptive or anxiety producing (*18*, *26*, *27*). However, the role of the LC in systemic opioid antinociception remains an open question, as the literature on this topic is sparse and conflicting (*28*, *29*).

Anatomical studies have identified projections from the PAG to the LC (*30*). Unexpectedly, the synaptic features of these projections and their relevance to pain modulation have not been established. Although a rabies tracing study reported inputs to spinally projecting LC-NA neurons from vlPAG, and a slice electrophysiology study found an excitatory connection from lateral PAG to LC-NA neurons (*31*–*33*), previous in vivo electrophysiological recordings reported only weak, sparse input that predominantly inhibits LC discharge (*34*). Furthermore, vlPAG→LC neurons were reported to be inhibited by mu opioids (*32*), which conflicts with the notion that vlPAG output can drive descending LC neurons in the context of opioid analgesia. Thus, whether vlPAG contributes to the activation of the LC to support opioid antinociception remains unclear.

An additional complexity relates to the potential role of the RVM in influencing pain processing via synaptic communication with the LC. One anatomical study reported projections from both the raphe magnus and paragigantocellular nucleus, both components of the medial RVM, to the LC and pericoerulear region (*35*), but the sign and functional significance of this anatomical pathway remains unexplored. There is a strong body of literature demonstrating antinociceptive input to LC from excitatory neurons in the rostral ventrolateral medulla (*36*, *37*) and, more recently, noradrenergic excitatory neurons in the caudal ventrolateral medulla (*38*). However, to our knowledge, there is no information regarding the nature and behavioral relevance of medial RVM inputs to the LC.

In this study, we use virally and genetically mediated anatomical, electrophysiological, and behavioral methods in mice to establish the circuit elements by which the DPMS recruits the LC to produce opioid antinociception. Our findings reveal the necessity of vlPAG input to the LC for systemic morphine antinociception and uncover an unexpected inhibitory input from the RVM that affects nociception. These findings emphasize the importance of noradrenergic

[1]Department of Neurobiology, School of Biological Sciences, University of California, San Diego, La Jolla, CA 92093, USA. [2]Neurosciences Graduate Program, University of California, San Diego, La Jolla, CA 92093, USA. [3]Biological Sciences Graduate Program, University of California, San Diego, La Jolla, CA 92093, USA. [4]Chemistry and Biochemistry Graduate Program, University of California, San Diego, La Jolla, CA 92093, USA. [5]Departments of Anesthesiology and Pharmacology, University of California, San Diego, La Jolla, CA 92093, USA.
*Corresponding author. Email: mbanghart@ucsd.edu

signaling from the LC in opioid analgesia and reveal a previously unappreciated antinociceptive pathway within the DPMS.

RESULTS

Spinal NA release from the LC underlies systemic morphine antinociception

Intrathecal pharmacological experiments in rats point to a role for spinal noradrenergic and serotonergic signaling in systemic morphine antinociception (*13*). We first set out to confirm that spinal NA contributes to systemic morphine antinociception in mice by administering multiple doses of systemic morphine [5, 12, and 20 mg/kg, subcutaneously (s.c.)] in conjunction with intrathecal injections of the vehicle saline, the α-adrenergic antagonist phentolamine (5 μg), or, for comparison, the opioid antagonist naltrexone (5 μg) (Fig. 1A). Systemic morphine with intrathecal saline administration increased hot plate hind paw withdrawal latencies in a dose-dependent manner (Fig. 1B). At all morphine doses, intrathecal phentolamine blunted the resulting antinociception, and intrathecal naltrexone reduced it to an even greater degree (Fig. 1, B and C). In this experiment and throughout this study, male and female mice were pooled, as no differences were observed between sexes. These results indicate that spinal NA plays a critical role in the expression of systemic morphine antinociception, especially at low doses of morphine. In contrast, spinal opioid signaling, whether via direct spinal actions of morphine or DPMS-driven endogenous opioid release (*39*, *40*), is required for systemic morphine antinociception at all doses.

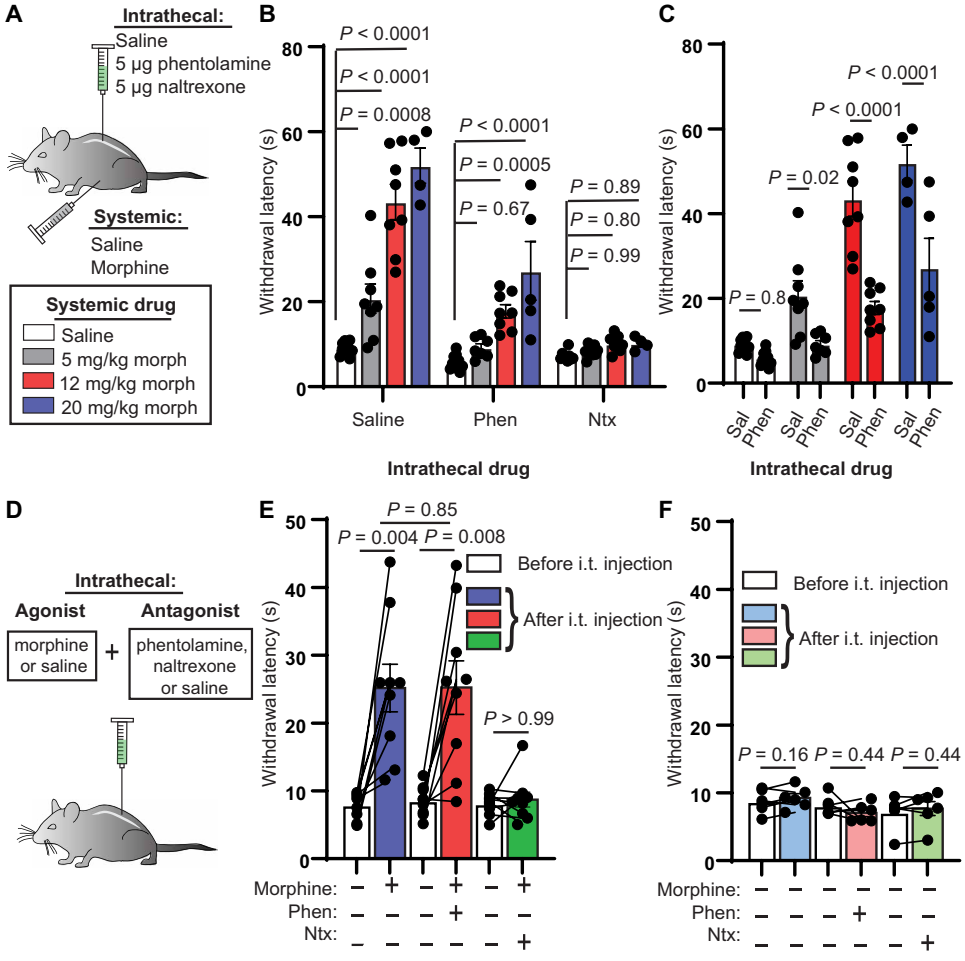

Fig. 1. Intrathecal noradrenergic and opioidergic antagonists attenuate systemic morphine antinociception. (**A**) Schematic of intrathecal and systemic injection combinations and morphine doses. (**B**) Hot plate withdrawal latencies resulting from increasing doses (0, 5, 12, and 20 mg/kg, s.c.) of morphine grouped by intrathecal antagonist [saline versus 5 μg of phentolamine versus 5 μg of naltrexone; ordinary two-way analysis of variance (ANOVA) with Tukey's multiple comparisons test; intrathecal drug effect, $P < 0.0001$, $F_{2,81} = 95.35$]. (**C**) Same data as in (B) from intrathecal saline and phentolamine groups reorganized by systemic morphine dose to facilitate comparisons (ordinary two-way ANOVA with Sidak's multiple comparisons test; intrathecal drug effect, $P < 0.0001$, $F_{1,52} = 63.07$). (**D**) Intrathecal coadministration of morphine (2.5 μg) or saline with saline, phentolamine, or naltrexone. (**E**) Hot plate withdrawal latencies before (white) and after (blue, saline; red, phentolamine; green, naltrexone) intrathecal (i.t.) injection of morphine and antagonist (pre- versus post-intrathecal injection, $n = 9$ pairs each, two-sided Wilcoxon matched-pairs signed rank test; post-intrathecal morphine + saline versus post-intrathecal morphine + phentolamine, $n = 9$ saline, $n = 9$ phentolamine, two-sided Mann-Whitney test). (**F**) Hot plate withdrawal latencies before (white) and after (light blue, saline; pink, phentolamine; light green, naltrexone) intrathecal injection of saline and antagonist (pre- versus post-intrathecal injection, $n = 6$ pairs each, two-sided Wilcoxon matched-pairs signed rank test). All graphs depict means ± SEM.

Direct spinal administration of morphine produces antinociception (*41*). It is therefore possible that morphine acts within the spinal cord to stimulate NA release either from descending noradrenergic terminals or from unidentified local NA neurons. To determine whether morphine-driven spinal NA signaling originates from a spinal or supraspinal source, we intrathecally administered morphine (2.5 μg) along with saline, phentolamine, or naltrexone, before the hot plate assay (Fig. 1D). Consistent with spinal NA arising from a supraspinal source, we found that the effect of intrathecal morphine was not blocked by intrathecal phentolamine, whereas intrathecal naltrexone blocked the antinociception (Fig. 1E). In the absence of morphine, these antagonists did not change withdrawal latencies (Fig. 1F).

Previous studies have identified several supraspinal noradrenergic structures that project to the dorsal horn of the spinal cord (*19*, *21*–*25*). Whereas the A5 and A7 nuclei contain only a small fraction of dorsal horn-projecting NA neurons, the LC is the primary source of spinal NA (*19*). Accordingly, stimulation of the spinally projecting ventral subdivision of LC produces spinal NA–dependent antinociception in mice and rats (*18*, *26*, *27*). To determine whether systemic morphine increases the activity of LC-NA neurons, we measured expression of the immediate early gene c-Fos in response to subcutaneous morphine (10 mg/kg) or saline treatment in *Dbh-cre::Ai14* mice that express the red fluorescent protein tdTomato in dopamine β-hydroxylase (DBH)–positive neurons. Consistent with LC activation, systemic morphine caused an increase in c-Fos expression in LC neurons that was attenuated by pretreatment with the opioid receptor antagonist naloxone (10 mg/kg, s.c.) (Fig. 2, A and B). This presents a paradox, as LC neurons are well known to express the mu opioid receptor (MOR), which typically inhibits neuronal output in receptor-expressing neurons (*42*–*44*). Using fluorescence in situ hybridization (FISH), we found that 93% of LC-NA neurons contain *Oprm1* transcripts in C57Bl6/J mice (fig. S1, A and B). A possible explanation is that the c-Fos induction results from direct engagement of mitogen-activated protein kinase cascades downstream of MOR activation (*45*). However, morphine-induced c-Fos expression was unchanged in *Dbh-cre::Oprm1*$^{fl/fl}$ mice (*46*), which lack MORs in NA neurons (fig. S1, C and D). To more directly measure activity in LC-NA neurons, we expressed GCaMP8s (*47*) in *Dbh-cre* mice and recorded intracellular Ca^{2+} using fiber photometry. In comparison to saline-injected controls, we observed a sustained increase in Ca^{2+} activity after morphine administration (10 mg/kg, s.c.) (Fig. 2, C to E). Together, these data suggest that LC activity is paradoxically increased by opioid administration. Because MORs expressed in LC neurons are not critical for morphine-induced c-Fos expression, LC activation is most likely mediated by opioid receptors present in upstream circuits through a synaptic mechanism.

We next sought to better understand the paradoxical activation of MOR-expressing LC-NA neurons by morphine. In rat brain slices, MOR agonists strongly hyperpolarize LC neurons via activation of G protein–coupled inward rectifier K^+ (GIRK) channels (*42*, *43*). Because nearly all previous observations of MOR-mediated dampening of LC neuronal excitability were made in rats, we asked whether mouse LC-NA neurons are similarly affected. We investigated the effects of the MOR agonist DAMGO on LC neuronal excitability using whole-cell electrophysiological recordings in acute mouse brain slices. Bath-applied DAMGO requires minutes to equilibrate in slices, which can obscure subtle effects on membrane properties. We therefore used the photocaged DAMGO derivative CNV-Y-DAMGO (1 μM) to produce time-locked DAMGO concentration jumps in response to millisecond flashes of light (*48*, *49*). In current clamp recordings, despite the use of a strong optical stimulus, CNV-Y-DAMGO photoactivation generated only small hyperpolarizations that were accompanied by brief pauses in spontaneous firing and minor subsequent reductions in firing rate (Fig. 2, F to I). In voltage clamp recordings, DAMGO photorelease evoked correspondingly small, brief outward currents (Fig. 2, F and J). Consistent with these modest effects, bath application of DAMGO (1 μM) did not alter evoked action potential firing (Fig. 2K). These small effects stand in stark contrast to the several-hundred picoampere currents and deep hyperpolarizations evoked by MOR agonists in rat LC and are consistent with the smaller GIRK currents previously observed in mice on a different genetic background (*50*). These results suggest that direct MOR-mediated inhibition of LC firing may be insufficient to counteract synaptic drive of LC neurons by upstream circuits in mice. Consistent with this notion, genetic removal of MORs from LC-NA neurons did not alter systemic morphine antinociception on the hot plate (fig. S1E).

To determine whether the LC contributes to morphine antinociception, we used two loss-of-function approaches. First, we specifically ablated LC-NA neurons via bilateral injection of AAV–DIO–Caspase 3 (Casp3) into the LC of either *Dbh-cre::Ai14* mice or control *Ai14* littermates. Cre-dependent transduction with Casp3 led to near-complete ablation of LC-NA neurons (Fig. 2L). In addition to assessing thermal nociception, we used a pin prick assay to measure mechanical nociception. Somewhat unexpectedly, LC ablation had no effect on baseline nocifensive responses in the absence of morphine. However, in comparison to control mice, the morphine-induced increase in hot plate withdrawal latency was strongly attenuated in *Dbh-cre::Ai14* mice at both doses of morphine (5 and 10 mg/kg). In addition, the morphine-induced decrease in pin prick response was significantly attenuated at 5 mg/kg morphine and trended toward significance at 10 mg/kg (Fig. 2M).

Casp3-mediated cell ablation is a severe manipulation that may lead to confounds due to neuroinflammation and/or a loss of structural integrity. We therefore sought to corroborate these findings using a milder loss-of-function approach. We chose to suppress LC activity by overexpressing Kir2.1, a constitutively active inwardly rectifying K^+ channel, which hyperpolarizes neurons and decreases their excitability. We first analyzed the effect of Kir2.1 overexpression on LC neuronal excitability using brain slice electrophysiology 3 weeks after unilateral LC injection of AAV-DIO-Kir2.1-zsGreen in *Dbh-cre* mice. Kir2.1 overexpression decreased resting membrane potential and abolished tonic action potential firing compared to anatomically identified LC neurons in the uninjected hemisphere (fig. S2, A and B). We also observed a decrease in evoked action potential firing in response to injection of 50- and 100-pA current steps (fig. S2C). Together, Kir2.1 overexpression effectively decreases both tonic and evoked action potential firing in LC neurons.

For behavioral testing, we bilaterally injected AAV-DIO-Kir2.1-zsGreen into the LC of *Dbh-cre:Ai14* or *Ai14* mice. Histological analysis revealed that ~80% of LC-NA neurons were transduced in cre-expressing mice, with negligible expression in cre-negative littermates (Fig. 2N). Similar to Casp3-mediated ablation, Kir2.1 overexpression suppressed morphine antinociception on both the hot plate and pin prick assays at both doses of morphine (Fig. 2O). Notably, neither Casp3 nor Kir2.1 produced a difference in locomotion

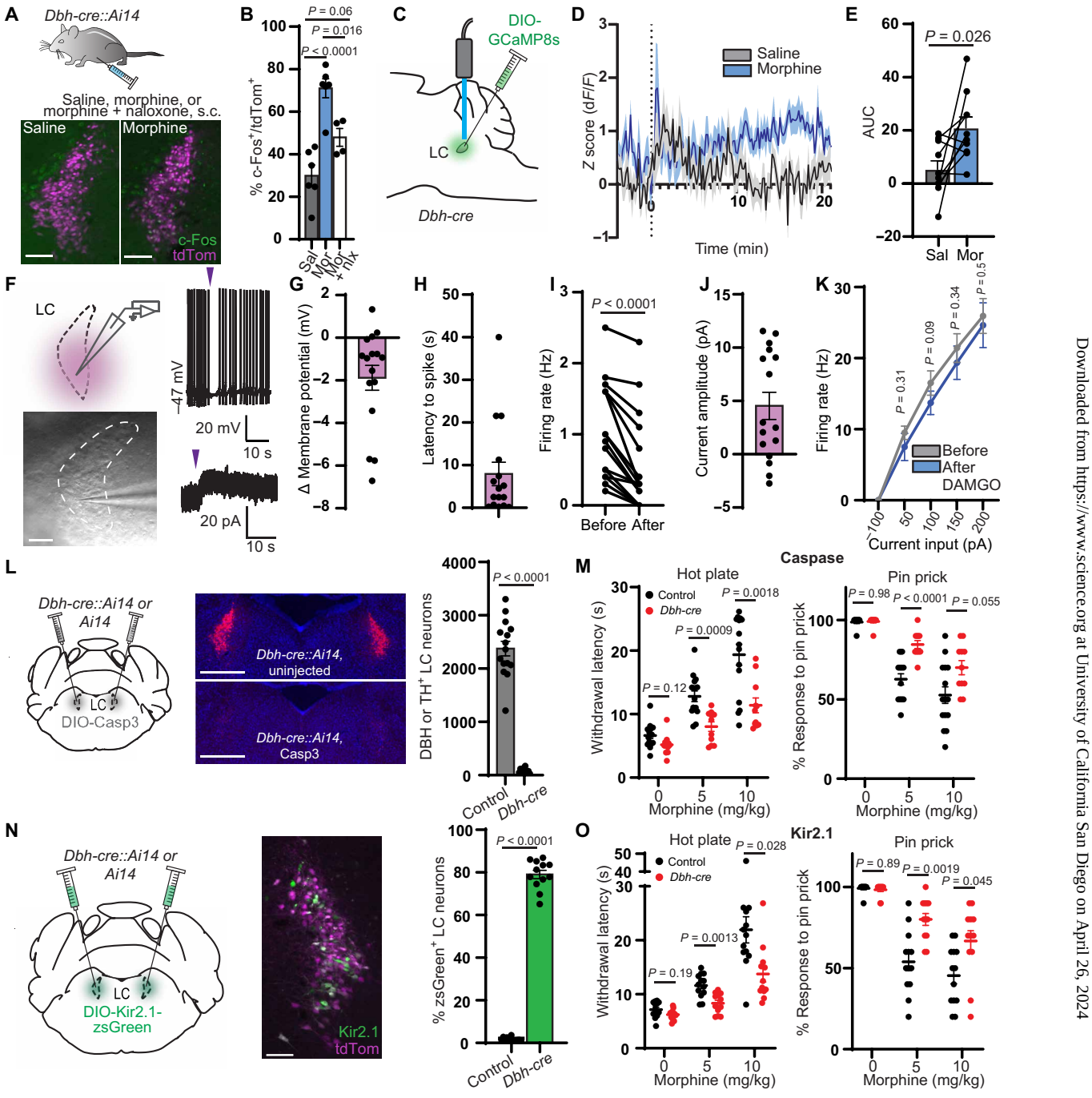

Fig. 2. LC activity is required for systemic morphine antinociception. (**A**) c-Fos expression after injection. Scale bars, 150 μm. (**B**) Percentage of LC neurons that colocalize with c-Fos (five to eight images per mouse; $n = 6$ saline, $n = 6$ morphine, $n = 4$ naloxone; one-way ANOVA with Tukey's multiple comparisons test, $P < 0.0001$, $F_{2,13} = 20.97$). (**C**) Injection of GCaMP8s and fiber implantation for fiber photometry. (**D**) Average normalized Ca^{2+} response to morphine or saline at time 0 ($n = 10$ mice). (**E**) Area under the curve (AUC) from 0 to 20 min (two-sided paired *t* test: $t = 2.652$, $n = 10$ pairs). (**F**) Left: Slice recordings from LC neurons with light-evoked uncaging. Scale bar, 150 μm. Right: Representative traces of CNV-Y-DAMGO uncaging (purple arrows, 50 ms; 365-nm LED, 84 mW) in current (top) and voltage clamp (bottom). (**G** to **J**) Response to CNV-Y-DAMGO uncaging ($n = 16$ cells). (G) Change in membrane potential. (H) Latency to spike after uncaging. (I) Tonic firing rate in the 10 s before and after uncaging ($P < 0.0001$, two-sided Wilcoxon matched-pairs signed rank test). (J) Outward current amplitude. (**K**) *f-I* curves before and after DAMGO bath application ($n = 7$ cells; two-sided Wilcoxon matched-pairs signed rank test at each current level). (**L**) Quantification of neuronal ablation by AAV-DIO-Casp3 (scale bars, 500 μm; $n = 11$ *Dbh-cre*, $n = 15$ control; two-sided Mann-Whitney test). (**M**) Left: Hot plate withdrawal latencies after morphine. Right: Response to 10 hind paw pin pricks ($n = 11$ *Dbh-cre*, $n = 15$ control; two-way repeated-measures ANOVA with Sidak's multiple comparisons test; hot plate: $P = 0.0006$, $F_{1,24} = 15.67$; pin: $P = 0.0006$, $F_{1,24} = 15.52$. (**N**) Representative image of zsGreen expression in the LC (scale bar, 150 μm) and quantification of viral coverage ($n = 12$ *Dbh-cre*, $n = 13$ control; two-sided Mann-Whitney test). (**O**) Same as (M) for Kir2.1 silencing ($n = 12$ *Dbh-cre*, $n = 13$ control; two-way repeated-measures ANOVA with Sidak's multiple comparisons test, hot plate: $P = 0.001$, $F_{1,23} = 14.30$; pin: $P = 0.0004$, $F_{1,23} = 17.20$). Data reported as means ± SEM.

or basal anxiety in the elevated plus maze (fig. S2, D and E). We confirmed that our viral injections did not transduce the neighboring A7 nucleus (fig. S2, F to I), which has been previously implicated in descending noradrenergic pain modulation in rats (*22*, *51*–*53*). Overall, these results support a critical role for the LC in systemic morphine antinociception.

vlPAG gates LC-mediated morphine antinociception

Although we have established that the LC is crucial for systemic morphine antinociception, it remains unclear how LC activity is recruited by upstream structures in response to opioid drugs. Classic models of opioid antinociception involve the disinhibition of vlPAG output neurons via activation of MORs expressed on inhibitory terminals and/or local γ-aminobutyric acid (GABA) neurons within the vlPAG (*3*, *5*). Consistent with this, the antinociception produced by local morphine infusion into rat PAG partially depends on spinal NA (*12*). Furthermore, several PAG subregions, including the vlPAG, send excitatory projections to the LC and pericoerulear region (*30*–*33*). Although optogenetic and chemogenetic activation of vlPAG glutamatergic neurons produces antinociception in mice (*54*, *55*), whether this is mediated by the LC, and whether vlPAG glutamatergic neurons support morphine antinociception, is not known.

If the vlPAG is an important upstream mediator of morphine antinociception, we reasoned that inhibiting vlPAG output should attenuate the antinociception produced by 5 mg/kg morphine, which we found to rely heavily on the LC. To probe the role of the vlPAG, we bilaterally expressed the inhibitory DREADD hM4Di (*56*) in vlPAG$^{Vglut2\text{-}cre}$ neurons and inhibited their output with systemic clozapine N-oxide (CNO) [3 mg/kg, intraperitoneally (i.p.)] in the absence and presence of morphine (5 mg/kg, s.c.) (Fig. 3A). Consistent

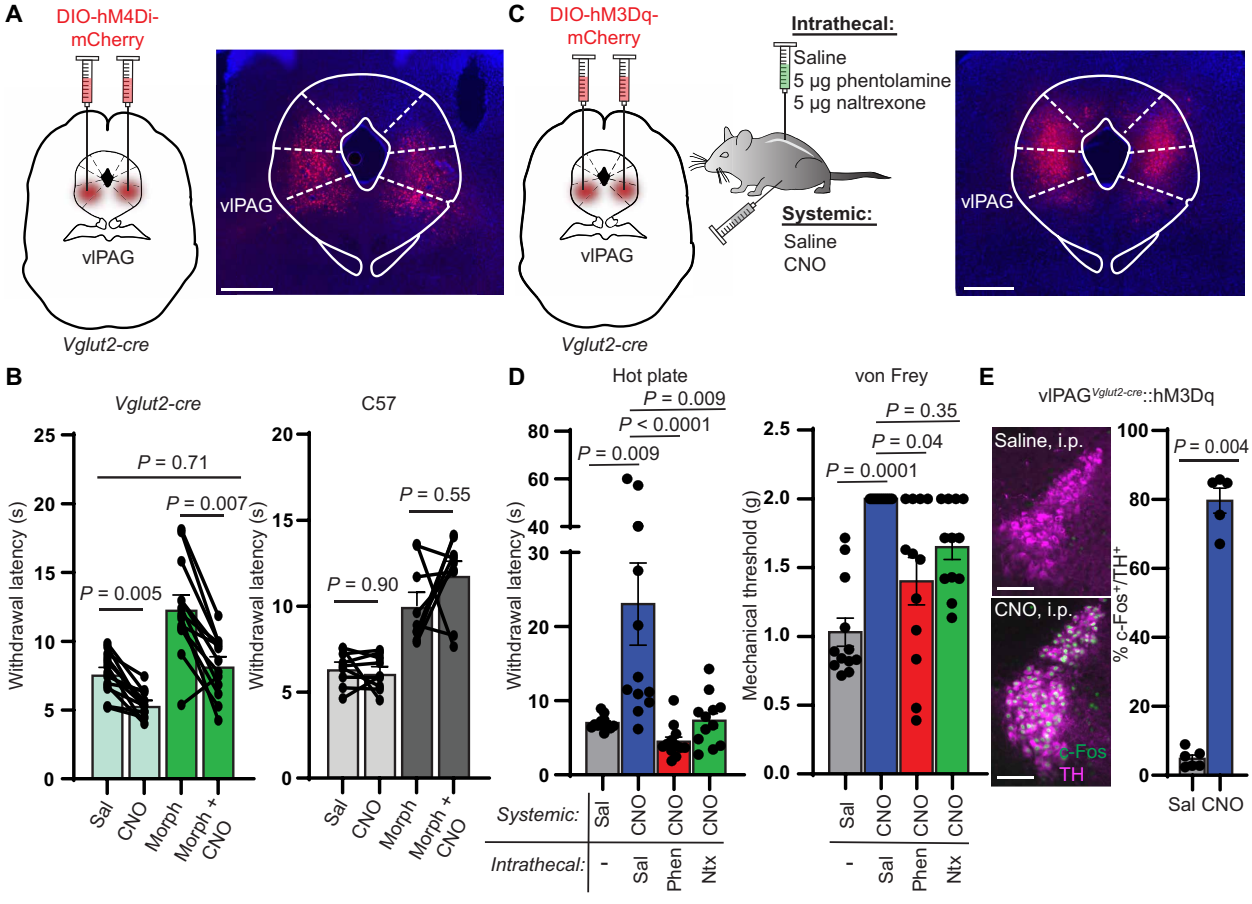

Fig. 3. vlPAG activity is required for systemic morphine antinociception and drives spinal NA–dependent antinociception. (**A**) Bilateral vlPAG AAV-DIO-hM4Di-mCherry injections in *Vglut2-cre* mice with representative image of viral expression. Scale bar, 500 µm. (**B**) Left: Hot plate withdrawal latencies of vlPAG$^{Vglut2\text{-}cre}$::hM4Di mice administered CNO (3 mg/kg i.p.) versus saline without (light green bars) and with morphine (5 mg/kg s.c.) (dark green bars) (two-way repeated-measures ANOVA with Tukey's multiple comparisons test; $n = 13$ mice; saline versus CNO effect, $P < 0.0001$, $F_{1,12} = 56.93$). Right: Withdrawal latencies of non–virus-injected controls (two-way repeated-measures ANOVA with Tukey's multiple comparisons test; $n = 9$ mice; saline versus CNO effect, $P = 0.32$, $F_{1,8} = 1.143$). (**C**) Bilateral vlPAG AAV-DIO-hM3Dq-mCherry injections in *Vglut2-cre* mice, combinations of systemic CNO with intrathecal antagonists, and representative image of viral expression. Scale bar, 500 µm. (**D**) Left: Withdrawal latencies after systemic saline or CNO and intrathecal saline, phentolamine (5 µg), or naltrexone (5 µg) (Friedman test with Dunn's multiple comparisons test, $n = 12$ subjects, $P < 0.0001$, Friedman statistic = 26.40). Right: Von Frey mechanical thresholds (Friedman test with Dunn's multiple comparisons test, $n = 12$ subjects, $P = 0.0001$, Friedman statistic = 21.00). (**E**) Representative images of c-Fos immunohistochemistry in TH-positive LC neurons of vlPAG$^{Vglut2\text{-}cre}$::hM3Dq mice after systemic injection of saline (top) or CNO (bottom). Scale bars, 150 µm. Right: % of TH-positive LC neurons that colocalize with green c-Fos signal (five to eight images analyzed per mouse; $n = 6$ saline, $n = 5$ CNO, two-sided Mann-Whitney test). Data in each graph reported as means ± SEM.

with our hypothesis that vlPAG activity is critical for triggering LC-mediated morphine antinociception, CNO completely prevented morphine antinociception in hM4Di-expressing mice but was without effect in untransduced control mice (Fig. 3B).

To determine whether spinal NA signaling mediates vlPAG-driven antinociception, we bilaterally activated vlPAG$^{Vglut2\text{-}cre}$ neurons with the excitatory DREADD hM3Dq in conjunction with intrathecal NA antagonism (Fig. 3C). Consistent with previous work (*55*), systemic CNO (3 mg/kg, i.p.) increased hot plate withdrawal latencies and von Frey mechanical thresholds. Strikingly, this effect was either completely or partially abolished on the thermal and mechanical assays, respectively, by intrathecal administration of either phentolamine or naltrexone (Fig. 3D). However, we also observed that chemogenetic activation of vlPAG$^{Vglut2\text{-}cre}$ neurons produced a state of active quiescence, in which mice exhibited a marked reduction in voluntary locomotion (fig. S3A). This raises a concern that the apparent antinociception is simply a consequence of general locomotor suppression. However, inconsistent with this explanation, the active quiescence persisted after intrathecal phentolamine and naltrexone administration, despite significant attenuation of the antinociception. This result reveals that vlPAG-driven descending antinociception and the concomitant locomotor suppression are dissociable, as only antinociception is dependent on spinal NA. Consistent with the vlPAG driving the LC to produce spinal NA–dependent antinociception, we also found that chemogenetic activation of vlPAG$^{Vglut2\text{-}cre}$ neurons increased c-Fos expression in tyrosine hydroxylase (TH)–positive LC neurons (Fig. 3E), yet CNO had no effect in the LC of untransduced control mice (fig. S3B). Together, these results demonstrate that, like systemic morphine, vlPAG-driven antinociception correlates with LC activation and requires spinal NA signaling. They also establish a role for spinal endogenous opioid signaling in vlPAG-driven antinociception, a point debated in previous literature (*9*, *40*, *57*).

Anatomy of DPMS input to the LC

To uncover the circuit elements by which the DPMS may recruit the LC, we first mapped projections from the vlPAG and RVM to the LC by virally expressing tdTomato in neurochemically defined cell types. To label glutamatergic neurons, we used *Vglut2-cre* mice, as VGLUT2 is the primary vesicular glutamate transporter isoform in both structures. To label inhibitory axons, we used *Vgat-cre* mice, which express cre in both GABAergic and glycinergic neurons (*58*).

After unilateral injection of AAV-DIO-tdTom into the vlPAG of either *Vglut2-cre* or *Vgat-cre* mice, we observed sparse fibers in the LC somatic region and strong labeling in the surrounding pericoerulear region that includes a dorsolateral zone and a medial zone that includes Barrington's nucleus (Fig. 4, A to G) (*59*). The dendrites of LC-NA neurons extend into this pericoerulear zone where vlPAG is known to make synaptic contact with neurons in Barrington's nucleus (*60*). Accordingly, injection of AAV-DIO-synaptophysin-GFP (green fluorescent protein), which marks presynaptic terminals, into the vlPAG of *Vglut2-cre* mice yielded strong synaptophysin expression in close proximity to the dendrites of TH$^+$ LC-NA neurons in the medial pericoerulear region as well as cell bodies in the LC proper (fig. S4, A and B). These findings provide evidence for putative monosynaptic connections between vlPAG axons and LC-NA neurons and are consistent with the presence of axo-dendritic inputs to LC-NA neurons occurring within the pericoerulear region (*61*). Furthermore, pericoerulear GABA neurons have recently been shown to provide synaptic input onto LC-NA neurons (*44*, *62*, *63*), which could support polysynaptic communication through this circuit.

As expected, tdTom expression in vlPAG$^{Vglut2\text{-}cre}$ neurons also yielded fluorescent axons in the RVM (fig. S4C). Somewhat unexpectedly, we also observed prominent fluorescent axons in the RVM upon tdTom expression in vlPAG$^{Vgat\text{-}cre}$ neurons (fig. S4D). The existence of inhibitory vlPAG→RVM projections has been established in rats but refuted in mice (*64*–*67*). We verified this inhibitory projection using a retro-FISH approach in which retrobeads were injected into the RVM before identification of retrobead-labeled vlPAG cell types using FISH (fig. S4E). This analysis revealed that although the vast majority of vlPAG→RVM projection neurons contain transcripts encoding glutamatergic (but not GABAergic) markers, ~15% contain only GABAergic markers (fig. S4F). These results establish that the vlPAG sends inhibitory projections to the RVM in mice.

We wondered whether vlPAG→LC neurons send branches to other brain areas. To address this question, we fluorescently labeled vlPAG neurons that project to the LC using the retrograde virus AAVretro-cre in wild-type mice (Fig. 4H). Consistent with our previous results, we observed mCherry-positive fibers in the medial pericoerulear region. However, we also observed prominent axon fibers in the RVM, with no other apparent midbrain and brainstem targets. This finding conflicts with a previous study in mice that reported the presence two molecularly distinct, nonoverlapping populations of vlPAG neurons that project either to the LC or the RVM (*32*). To confirm our result, we labeled vlPAG→RVM neurons using the same approach and again observed fluorescent axons in the medial pericoerulear region (Fig. 4I). We further verified these findings using a dual-color double-retrograde approach by injecting AAVretro-cre into the RVM, AAVretro-FlpO into the LC, and a mixture of cre- and flp-dependent mCherry and yellow fluorescent protein (YFP) reporter viruses in the vlPAG. The reporter virus titers were optimized to eliminate recombinase-independent expression and/or apparent recombinase cross-talk. Strikingly, we observed mCherry and YFP coexpression in 31% of fluorescently labeled neurons (Fig. 4J), which is likely an underestimate due to incomplete viral uptake in the injection zone. Injection of AAVretro-DIO-FlpO into either the RVM or LC, and AAV-fDIO-YFP in the vlPAG of *Vglut2-cre* mice verified that vlPAG glutamatergic neurons send bifurcating projections to the RVM and LC (fig. S4, G and H). Together, these experiments establish that a large number of vlPAG output neurons send bifurcating axons to both the LC and RVM. Given their glutamatergic nature, these results imply that vlPAG recruits the LC and RVM in an inseparable, parallel manner.

We next asked whether we could detect projections from the RVM to the LC, which were reported in only a single previous study (*35*). Upon injecting AAV-DIO-TdTom into the RVM of *Vglut2-cre* or *Vgat-cre* mice, red fluorescent fibers were found in the LC and pericoerulear region in innervation patterns distinct from vlPAG axons (Fig. 5, A to G). Notably, RVM$^{Vglut2\text{-}cre}$ axons were sparse within the LC somatic and medial pericoerulear regions, did not innervate Barrington's nucleus, and innervated a region just lateral to the LC. In contrast, RVM$^{Vgat\text{-}cre}$ axons appeared to strongly innervate the LC somatic zone and symmetrically spill over only slightly into the medial and lateral pericoerulear regions. In addition, analysis of fibers from all four projection origin and cell type combinations along the dorsal-ventral (DV) axis within the LC somatic

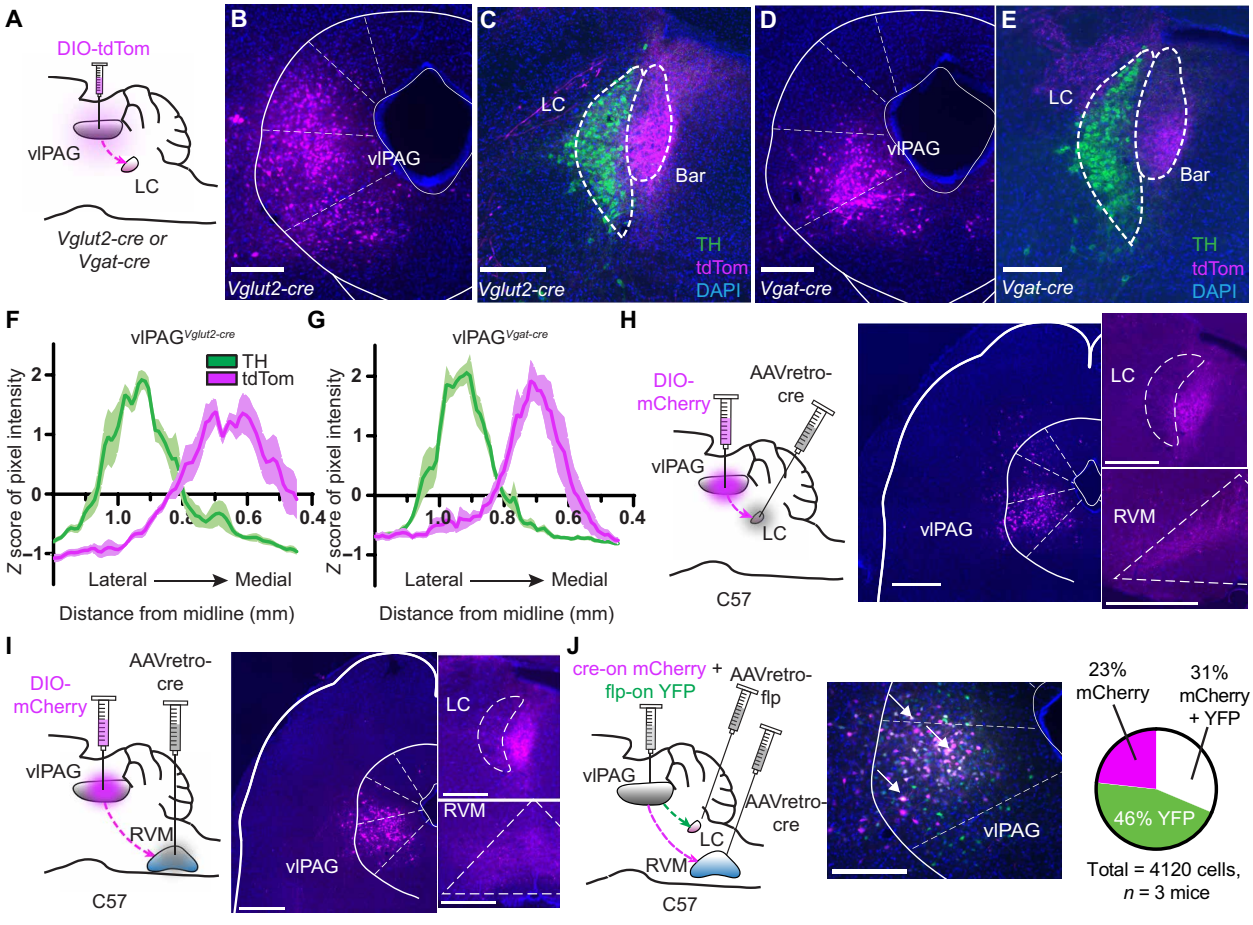

Fig. 4. Anatomical characterization of inputs to the LC from the vlPAG. (**A**) vlPAG injection of AAV-DIO-tdTom in *Vglut2*- or *Vgat-cre* mice. (**B**) *Vglut2-cre* injection site. (**C**) vlPAG$^{Vglut2\text{-}cre}$ terminals (magenta) and TH (green) in the peri-LC. Bar, Barrington's nucleus. (**D**) *Vgat-cre* injection site. (**E**) vlPAG$^{Vgat\text{-}cre}$ terminals. Scale bars, 300 μm [(B) to (E)]. (**F**) Quantification of magenta and green pixel intensity in the peri-LC of vlPAG$^{Vglut2\text{-}cre}$::tdTom mice normalized by *z* score ($n = 6$ LC slices from three mice). (**G**) Same as (F) for vlPAG$^{Vgat\text{-}cre}$::tdTom. (**H**) Left: Injections of AAVretro-cre in the LC and AAV-DIO-mCherry in the vlPAG of wild-type mice. Middle: Image of mCherry^{+} vlPAG neurons. Right: Resulting terminals in the LC and RVM. Scale bars, 500 μm. (**I**) Same as (H) for vlPAG→RVM neurons. Scale bars, 500 μm. (**J**) Left: Orthogonal recombinase strategy to label vlPAG neurons that project to the RVM and LC. Middle: Representative image of mCherry (magenta) and YFP (green). Arrows indicate double-labeled (white) neurons. Scale bar, 300 μm. Right: Quantification of mCherry and YFP in the vlPAG.

region suggested that vlPAG largely targets the dorsal LC, whereas RVM preferentially targets the ventral LC (Fig. 5H).

To determine whether RVM→LC neurons send branching axons to other structures, we injected AAVretro-cre in the LC and AAV-DIO-tdTom in the RVM and looked for axons throughout the nervous system (Fig. 5, I and J). Most prominent was a dense projection to the parafascicular nucleus of the thalamus, which also receives input from the LC (Fig. 5, K and L) (*68*). Notably, we did not find fluorescent axons in the spinal cord dorsal horn (Fig. 5M), indicating that RVM→LC projection neurons belong to a population distinct from the spinally projecting RVM neurons that directly modulate incoming noxious sensory information. Together, these results suggest that the LC receives neurochemically diverse synaptic inputs from multiple hindbrain nodes within the DPMS.

The presence of RVM→LC neurons raises the possibility that the vlPAG might influence the LC through the convergence of direct (vlPAG→LC) and indirect (vlPAG→RVM→LC) pathways. To assess this possibility, we used a dual anterograde and retrograde viral tracing approach. To label RVM neurons that receive synaptic input from the vlPAG, we injected the anterograde viral tracer scAAV1-cre (*69*, *70*) in the vlPAG. To label RVM→LC neurons, we injected AAVretro-DIO-GFP into the LC in the same mice such that RVM→LC neurons that receive synaptic input from the vlPAG should be transduced by both viruses and express GFP. Although injection of scAAV1-cre into the vlPAG of *Ai14* reporter mice yielded anterogradely labeled RVM neurons (fig. S5, A to C), we did not observe any GFP-positive cell bodies in the RVM (fig. S5, D and E) of doubly injected mice. Instead, we only observed GFP-expressing axons, presumably arising from vlPAG neurons that project to both the LC and RVM (fig. S5F). Although these negative results are not unequivocal, they suggest that RVM→LC neurons are not under the direct control of the vlPAG.

Synaptic properties of vlPAG and RVM input to the LC

To determine whether vlPAG and RVM axons make functional synaptic connections onto LC-NA neurons, we recorded optogenetically evoked synaptic transmission using brain slice electrophysiology. We biased our recordings toward the spinally projecting population by

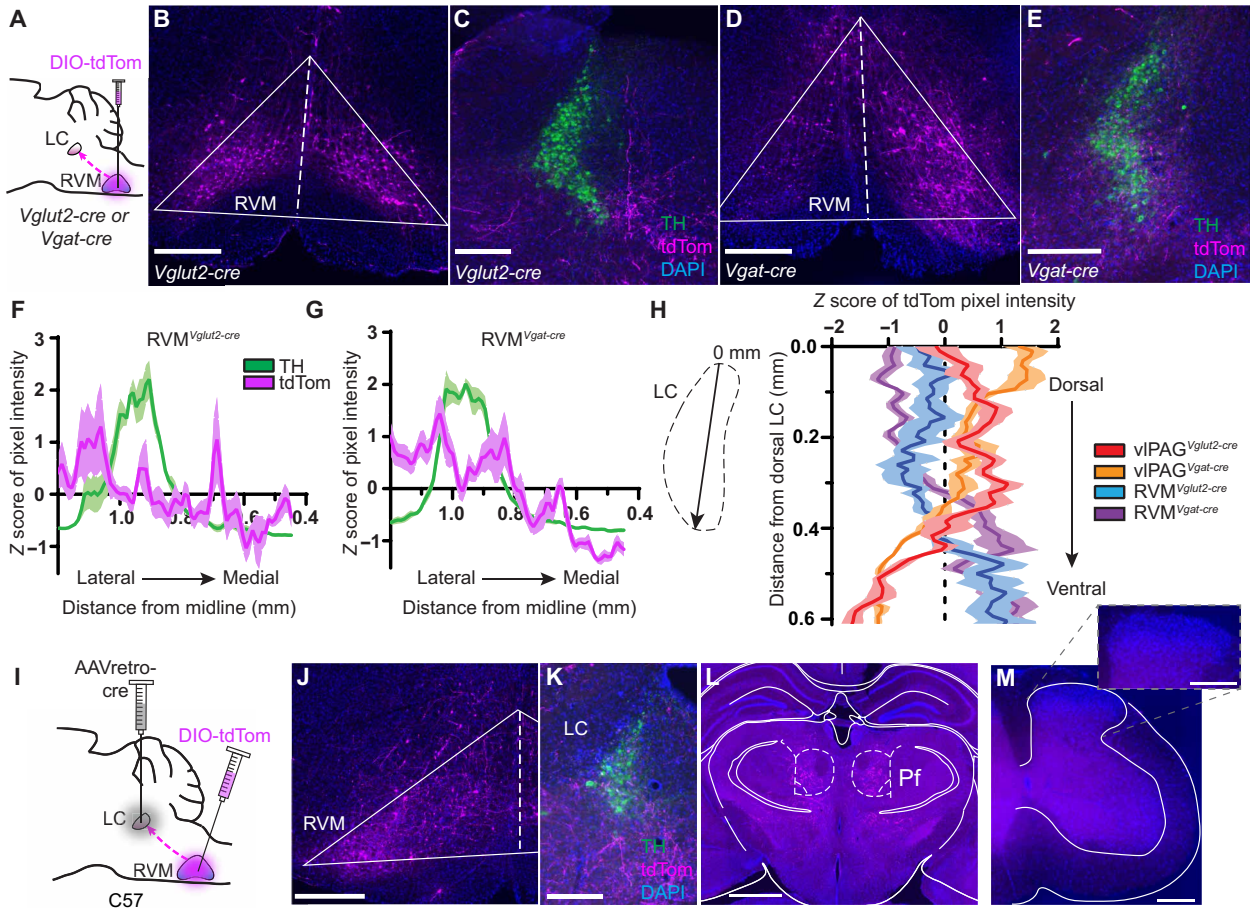

Fig. 5. Anatomical characterization of inputs to the LC from the RVM. (**A**) RVM injection of AAV-DIO-tdTom in *Vglut2-* or *Vgat-cre* mice. (**B**) *Vglut2-cre* injection site. (**C**) RVM$^{Vglut2\text{-}cre}$ terminals (magenta) and TH (green) in the peri-LC. (**D**) *Vgat-cre* injection site. (**E**) RVM$^{Vgat\text{-}cre}$ terminals. Scale bars, 300 μm (B to E). (**F**) Quantification of magenta and green pixel intensity in the peri-LC of RVM$^{Vglut2\text{-}cre}$::tdTom mice normalized by *z* score ($n = 6$ LC slices from three mice). (**G**) Same as (F) for RVM$^{Vgat\text{-}cre}$::tdTom. (**H**) Quantification of terminal intensity across the somatic LC DV axis for all projection origin and cell type combinations ($n = 6$ LC slices from three mice each). (**I**) Injections of AAVretro-cre in the LC and AAV-DIO-tdTom in the RVM of wild-type mice. (**J**) tdTom$^+$ RVM neurons. (**K**) Resulting terminals in the LC and peri-LC. Scale bars, 300 μm [(J) and (K)]. (**L**) tdTom$^+$ fibers in the bilateral thalamic parafascicular nucleus. Scale bar, 1 mm. (**M**) Representative lumbar spinal section. Inset: Zoom in of the dorsal horn. Scale bars, 300 μm.

targeting LC-NA neurons that were located in the ventral half of the LC (*19*). We visually identified LC-NA neurons based on their large, densely packed somata that are distinctly clustered just ventral to the ventrolateral corner of the fourth ventricle in coronal slices. All recorded neurons exhibited spontaneous action potential firing at ~1.5 Hz at 32°C. Confirming our ability to visually identify LC-NA neurons, we found that photoactivation of caged NA produced outward, α-adrenoreceptor–mediated inhibitory postsynaptic currents (IPSCs) in all neurons examined, similar to previous studies (fig. S6, A to E) (*33*, *44*, *71*). To achieve high expression of channelrhodopsin (ChR2) in all projection cell types, we injected wild-type mice in either the vlPAG or RVM with a combination of AAV-mCherry-IRES-cre and AAV-DIO-ChR2-mCherry, and obtained whole-cell recordings 3 to 4 weeks later.

We first determined the net effect of optogenetic axon stimulation on LC neuron firing using a 2-s blue light stimulus (2 ms, 25 Hz). Upon activating vlPAG inputs, we observed a firing rate increase in ~80% of recorded neurons, whereas ~20% showed no substantial change. Across the population, this resulted in an overall increase in firing rate during the stimulus (Fig. 6, A and B). In contrast, upon activating RVM inputs to LC, we observed a firing rate increase in only ~10% of the recorded neurons and a decrease in ~60%, whereas ~30% were not modulated. Across the population, this resulted in an overall decrease in firing rate (Fig. 6, C and D).

To gain insight into the synapses driving these changes in action potential firing, we measured optically evoked postsynaptic currents in voltage clamp recordings. To electrically isolate optogenetically evoked excitatory and inhibitory postsynaptic currents (oEPSCs and oIPSCs), we applied light while holding neurons at both −70 and 0 mV, respectively. Upon stimulating vlPAG axons (1 × 5-ms pulse), we detected oEPSCs in 30 of 36 neurons. Seven of these 30 neurons also responded with oIPSCs, but we did not observe any neurons displaying oIPSCs only. The relative oEPSC and oIPSC peak amplitudes are consistent with the overall excitatory drive from vlPAG observed in current clamp (Fig. 6E). On the other hand, upon stimulating RVM axons, we found oEPSCs in 32 of 72 neurons and oIPSCs

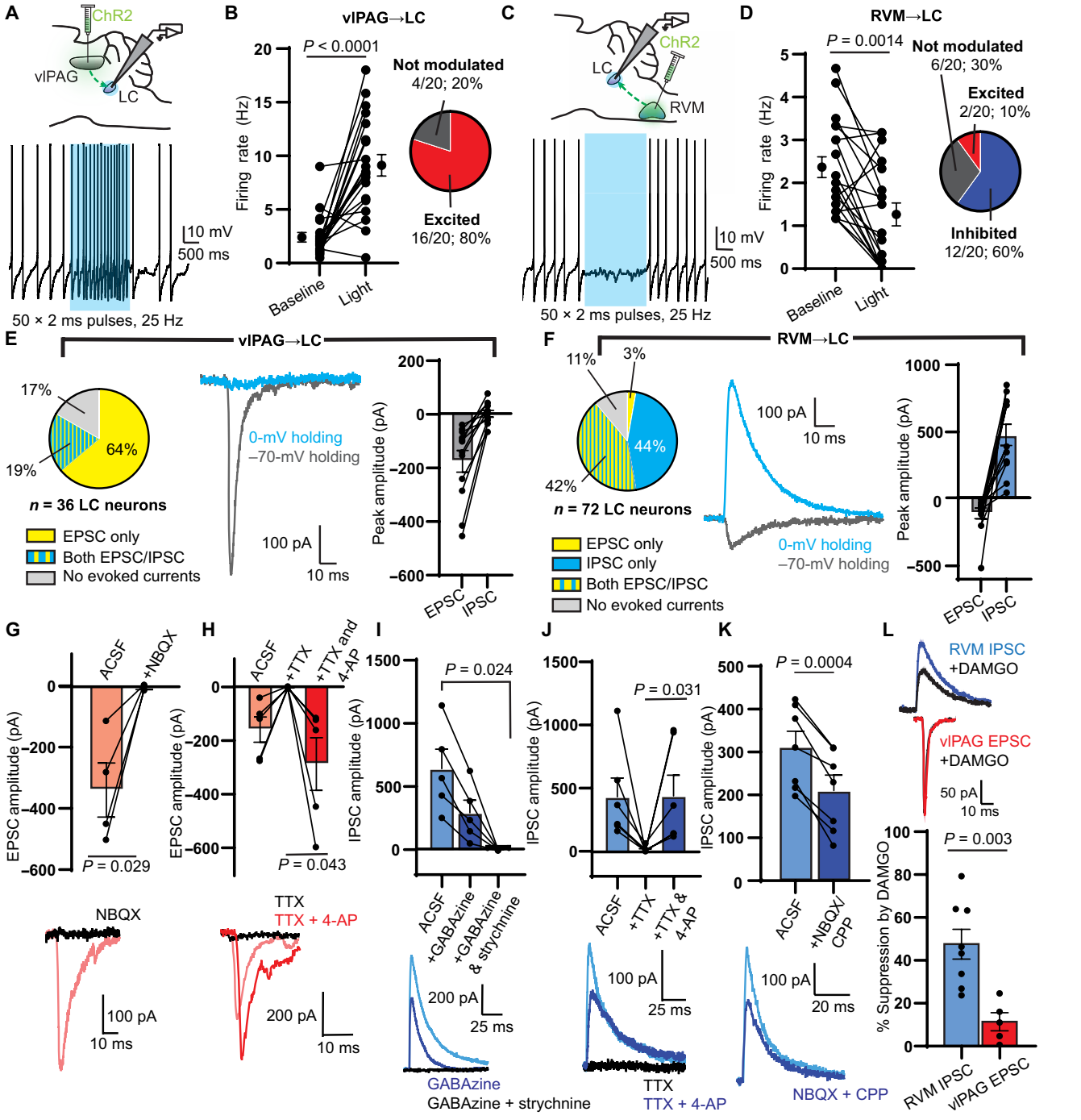

Fig. 6. Electrophysiological characterization of inputs from the vlPAG and RVM to the LC. (**A**) Top: vlPAG ChR2 viral injection for LC slice electrophysiology. Bottom: Representative trace of tonic spiking during a 2-s blue LED stimulus (470 nm, 50 × 2-ms pulses, 25 Hz, 18 mW). (**B**) Left: Firing rate before and during the stimulus ($n = 20$ neurons; two-sided Wilcoxon matched-pairs signed rank test). Right: Categorization of neurons as "excited" (z score of spiking during versus before light > 2), "inhibited" (z score < −2), or "not modulated." (**C**) Same as (A) for ChR2 expressed in the RVM. (**D**) Same as (B) for RVM terminal stimulation ($n = 20$ neurons; two-sided Wilcoxon matched-pairs signed rank test). (**E**) Left: Proportion of LC neurons with oEPSCs and oIPSCs during vlPAG terminal stimulation (1 × 5-ms pulse, 18 mW). Middle: Representative example of an oEPSC and oIPSC in a single LC neuron. Right: Peak amplitude of oEPSCs and oIPSCs ($n = 12$ neurons). (**F**) Same as (E) for RVM terminal stimulation ($n = 12$ neurons). (**G** to **K**) Top: Summary bar graphs of oEPSC/IPSC amplitude. Bottom: Representative examples. (G) NBQX effect on vlPAG oEPSC amplitude (two-sided paired t test: $t = 3.950$, $n = 4$ pairs). (H) TTX and 4-AP effect on vlPAG oEPSC amplitude (two-sided paired t test: $t = 2.926$, $n = 5$ pairs). (I) Effect of GABAzine and strychnine on RVM oIPSC (repeated-measures one-way ANOVA with Dunnett's multiple comparisons test, $P = 0.013$, $F_{1.087,4.348} = 16.32$, $n = 5$ cells). (J) Same as (H) for RVM oIPSCs (two-sided Wilcoxon matched-pairs signed rank test, $n = 6$ pairs). (K) Effect of NBQX and CPP on RVM oIPSC amplitude (two-sided paired t test: $t = 6.976$, $n = 7$ pairs). (**L**) Top: Examples of RVM oIPSCs (blue) and vlPAG oEPSCs (red) after bath application of DAMGO (1 μM; black). Bottom: Opioid sensitivity reported as % suppression of amplitude (two-sided unpaired t test: $t = 3.785$, $n = 8$ RVM oIPSC, $n = 5$ vlPAG oEPSC). All summary data reported as means ± SEM.

in 62 of 72 neurons, while 30 of 72 LC neurons exhibited both. The relative oEPSC and oIPSC peak amplitudes are consistent with the observed net inhibition of LC (Fig. 6F).

We next used pharmacology to dissect the underlying synaptic receptors, assess the presence of mono- and/or poly-synaptic connections, and evaluate the mu opioid sensitivity of each pathway. Consistent with a glutamatergic, monosynaptic excitatory connection, vlPAG-driven oEPSCs were blocked by the AMPA receptor antagonist 2,3-dihydroxy-6-nitro-7-sulfamoylbenzo[f]quinoxaline (NBQX; 10 μM) and completely abolished by the voltage-gated sodium channel blocker tetrodotoxin (TTX; 1 μM) but could subsequently be rescued by application of the voltage-gated potassium channel antagonist 4-aminopyridine (4-AP; 100 μM) (Fig. 6, G and H). Indicative of a mixed GABAergic and glycinergic projection, RVM-driven oIPSCs were partially blocked by the GABA-A receptor antagonist GABAzine (20 μM) and fully blocked by subsequent addition of the glycine receptor antagonist strychnine (10 μM) (Fig. 6I). Demonstrating the presence of a monosynaptic inhibitory connection, the oIPSCs were abolished and restored by TTX and 4-AP, respectively (Fig. 6J). However, bath application of NBQX and the *N*-methyl-D-aspartate (NMDA) antagonist carboxypiperazin-4-yl-propyl-1-phosphonic acid (CPP) (10 μM each) significantly decreased the oIPSC amplitude, suggesting the presence of an additional feed-forward, polysynaptic inhibitory component (Fig. 6K), which could be mediated by pericoerulear interneurons (*44*, *62*, *63*).

Last, we assayed the opioid sensitivity of vlPAG-driven oEPSCs and RVM-driven oIPSCs by bath applying DAMGO (1 μM) (Fig. 6L). Whereas vlPAG-driven oEPSCs were only slightly suppressed, RVM-driven oIPSCs were strongly attenuated. This suggests that in the presence of opioids, vlPAG excitatory drive to the LC remains largely intact, whereas suppression of inhibitory synaptic transmission from the RVM is poised to disinhibit LC neurons.

LC, vlPAG→LC, and RVM→LC neurons respond to noxious stimuli

To determine whether the vlPAG and RVM might convey pain-related information to the LC, we measured noxious stimulus–evoked Ca^{2+} activity in LC neurons and their primary inputs from the vlPAG and RVM using fiber photometry. After viral expression of GCaMP in either LC-NA neurons, glutamatergic vlPAG→LC neurons, or GABAergic/glycinergic RVM→LC neurons and unilateral optical fiber implantation (Fig. 7, A, E, and I), we applied noxious stimuli to the contra- and ipsilateral hind paws using either a Hargreaves apparatus (heat via a radiant heat light source set to 50% intensity) (Fig. 7, B, F, and J), a drop of acetone (cold via rapid evaporation) (Fig. 7, C, G, and K), or a pin prick (mechanical) (Fig. 7, D, H, and L). For comparison, we applied nonnoxious stimuli in the form of a 10% intensity beam in the Hargreaves test, room temperature water in the acetone drop test, and a 0.16-g von Frey filament in the pin prick test.

On the Hargreaves apparatus, the 50% light intensity setting produced a paw withdrawal with an average latency between 2.5 and 3.5 s for each experimental group, whereas the relatively nonnoxious 10% intensity did not induce an obvious withdrawal response for at least 10 s. In both cases, LC neurons, labeled with AAV-DIO-GCaMP8s in *Dbh-cre* mice, exhibited a large, transient (~1.5 s) response to the onset of the visible light stimulus. Because the light takes several seconds to heat the glass floor of the Hargreaves apparatus to noxious temperatures, we interpret this as a "salience signal," which has been observed in the LC in multiple contexts (*72*–*75*). Subsequently, Ca^{2+} activity in LC-NA neurons increased in response to the 50% intensity thermal stimulus until the time of paw withdrawal and then quickly decayed back to baseline. In contrast, the 10% intensity stimulus did not produce an increase in Ca^{2+} after cessation of the salience signal (Fig. 7B). Similarly, presentation of a noxious acetone drop produced a larger Ca^{2+} response than room temperature water (Fig. 7C), as did application of a pin prick in comparison to light touch with a nonnoxious von Frey filament (Fig. 7D). We observed large Ca^{2+} responses from the hind paws ipsi- and contralateral to the optical fiber and therefore pooled the data. Together, these results suggest that the LC responds not only to salient stimuli but also strongly to distinctly noxious stimuli. Whereas the salience and noxious stimulus responses are temporally resolved in the Hargreaves assay, they are likely superimposed in the acetone drop and pin prick assays due to the immediate and transient nature of noxious stimulus presentation.

We labeled glutamatergic vlPAG→LC neurons with GCaMP6m by injecting AAVretro-FlpO into the LC and AAV-Con/Fon-GCaMP6m (*76*, *77*) into the vlPAG of *Vglut2-cre* mice (Fig. 7E). Similarly to LC neurons, vlPAG$^{Vglut2\text{-}cre}$→LC neurons exhibited an immediate Ca^{2+} response to light onset in the Hargreaves assay, regardless of intensity. Distinctly, the Ca^{2+} response to the 50% intensity thermal stimulus continued to increase until the paw withdrawal occurred, and remained elevated for tens of seconds after noxious stimulus offset while the mouse continued to display nocifensive behaviors (Fig. 7F). In response to the 10% thermal stimulus, vlPAG$^{Vglut2\text{-}cre}$→LC Ca^{2+} activity returned to baseline after a brief salience response and slowly increased over the next several seconds, which may correspond to the increasing temperature of the apparatus floor. In response to the noxious acetone and nonnoxious water drops, Ca^{2+} activity in vlPAG$^{Vglut2\text{-}cre}$→LC neurons was graded in magnitude, similar to the observation in LC neurons, but longer lasting, as was observed in the Hargreaves assay (Fig. 7G). Similar trends were observed in the pin prick assay (Fig. 7H).

To record Ca^{2+} activity in inhibitory RVM→LC neurons, we injected AAV-DIO-GCaMP8s into the RVM of *Vgat-cre* mice and implanted an optical fiber in LC where it could measure fluorescence from their axons and presynaptic terminals (Fig. 7I). As with LC-NA neurons and vlPAG$^{Vglut2\text{-}cre}$→LC neurons, RVM$^{Vgat\text{-}cre}$→LC axons exhibited a transient response to the light onset in the Hargreaves assay, followed by a larger increase in response to the 50% intensity stimulus than the 10% intensity stimulus (Fig. 7J). Similar to vlPAG$^{Vglut2\text{-}cre}$→LC neurons, this response was longer lasting than in LC-NA neurons. Similar trends were also observed in the acetone drop and pin prick assays (Fig. 7, K and L).

In summary, LC-NA neurons, vlPAG$^{Vglut2\text{-}cre}$→LC projections, and RVM$^{Vgat\text{-}cre}$→LC projections all exhibit characteristic responses to a variety of noxious stimuli. All three circuit elements exhibit a salience response to stimulus onset, which is underscored by the fact that the visible thermal stimulus is not immediately noxious in the Hargreaves assay. In all cases, noxious stimulus–evoked Ca^{2+} activity was larger than that evoked by nonnoxious stimuli, across both sensory modalities (temperature and touch). However, the responses in each neuron class were temporally distinct, as Ca^{2+} activity in both vlPAG$^{Vglut2\text{-}cre}$→LC neurons and RVM$^{Vgat\text{-}cre}$→LC neurons outlasted LC activity by at least several seconds. These results are consistent with the notion that noxious stimulus–evoked activity in vlPAG and RVM shapes activity in LC-NA neurons but

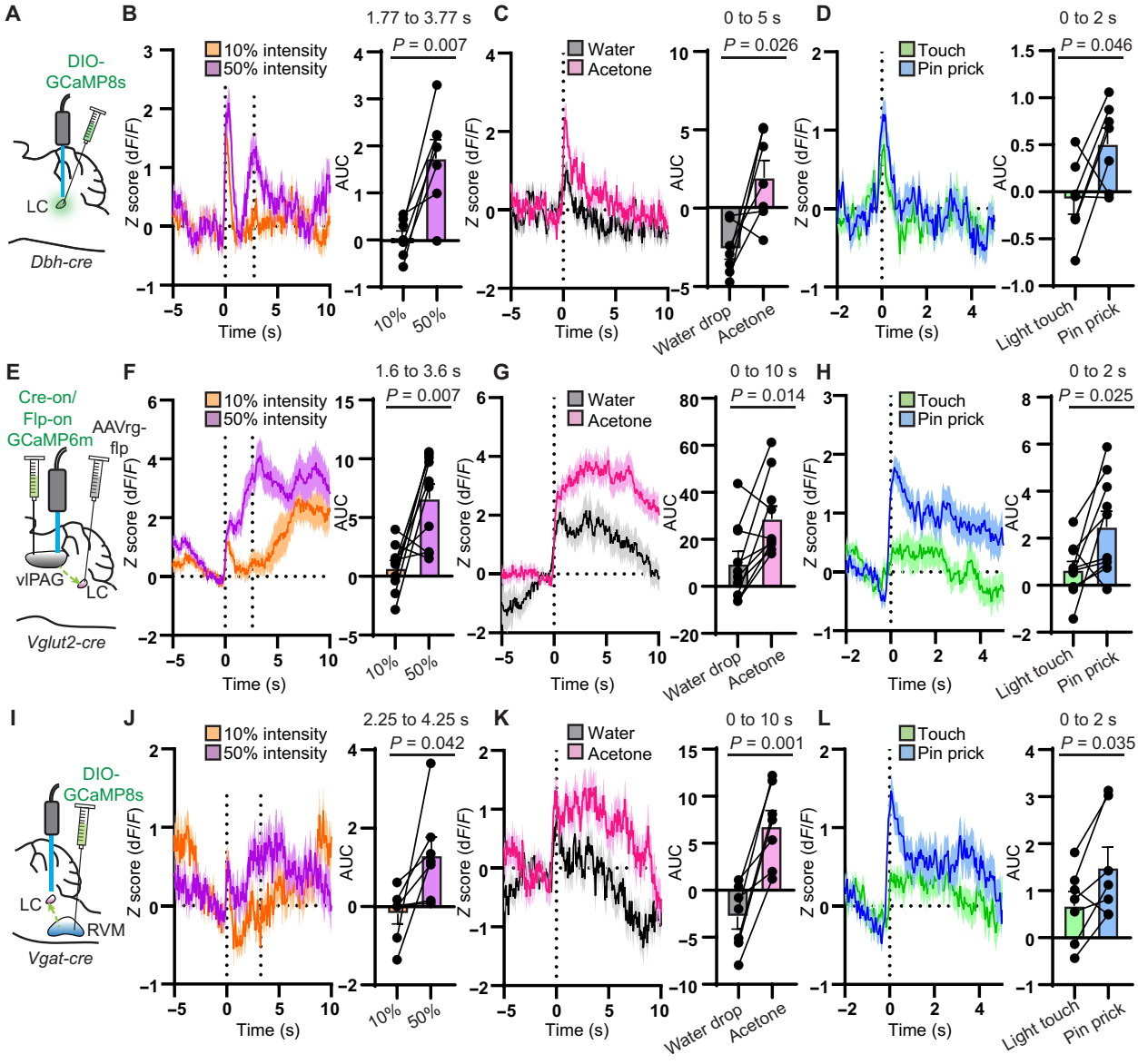

Fig. 7. LC, vlPAG→LC, and RVM→LC neurons are responsive to noxious stimuli. (**A**) Injection of AAV-DIO-GCaMP8s in *Dbh-cre* mice and fiber placement in the right LC. (**B**) Left: Normalized fluorescence change during the Hargreaves assay at 10% (orange) and 50% (purple) light intensity with light on at $t = 0$ s. The average withdrawal response to 50% intensity occurred at 2.77 s ($n = 7$ mice, 6 trials each). Right: AUC analysis per mouse from 1 s before to 1 s after the paw withdrawal (two-sided paired t test: $t = 4.012$). (**C**) Left: Fluorescence response to acetone or room temperature water on the hind paw ($n = 7$ mice, 4 trials each). Right: AUC analysis from 0 to 5 s (two-sided paired t test: $t = 2.944$). (**D**) Left: Fluorescence response to light touch with a 0.16-g von Frey fiber versus pin prick ($n = 7$ mice, 6 trials each). Right: AUC analysis from 0 to 2 s (two-sided paired t test: $t = 2.510$). (**E**) Injection of AAVretro-FlpO in the LC of *Vglut2-cre* mice and Cre-on/Flp-on GCaMP6m with fiber over right PAG. (**F**) Same as (B) for vlPAG→LC neurons. Average withdrawal at 2.60 s ($n = 10$ mice, 6 trials each; two-sided paired t test: $t = 3.507$). (**G**) Same as (C) for vlPAG→LC. AUC analysis taken from 0 to 10 s ($n = 10$ mice, 4 trials each; Wilcoxon matched-pairs signed rank test). (**H**) Same as (D) for vlPAG→LC ($n = 10$ mice, 6 trials each; two-sided paired t test: $t = 2.698$). (**I**) Injection of AAV-DIO-GCaMP8s in the RVM of *Vgat-cre* mice with fiber over right LC. (**J**) Same as (F) for RVM→LC terminals. Average withdrawal at 3.25 s ($n = 7$ mice, 6 trials each; two-sided paired t test: $t = 2.570$). (**K**) Same as (G) for RVM→LC terminals ($n = 7$ mice, 4 trials each; two-sided paired t test: $t = 5.646$). (**L**) Same as (H) for RVM→LC terminals ($n = 7$ mice, 6 trials each; two-sided paired t test: $t = 2.721$). Graphs represent means ± SEM.

does not establish a causal role for these synaptic pathways in pain modulation.

vlPAG and RVM inputs to LC modulate nociception

We next aimed to determine how these synaptic pathways shape nociception and how they contribute to systemic morphine antinociception. Because of the prominence of branching axons, we used a chemogenetic loss-of-function strategy that restricts inhibition to synaptic terminals in target structures via CNO infusion through implanted cannulas (*78*). We first investigated the contribution of vlPAG output to the LC. After bilateral injection of AAV-DIO-hM4Di-mCherry into the vlPAG of *Vglut2-cre* mice and 3 weeks of expression, we bilaterally implanted injected mice and control uninjected wild-type mice with cannulas over the LC. Following recovery,

mice were tested on the hot plate after bilateral infusion of either saline or CNO (3 μM), both in an opioid-naïve state and after injection of morphine (5 mg/kg, s.c.). In wild-type mice, intra-LC infusion of CNO had no effect either in the absence or presence of morphine (Fig. 8A). In vlPAG$^{Vglut2\text{-}cre}$::hM4Di mice, although intra-LC infusion of CNO did not alter baseline nociception, it produced a large, partial reduction in systemic morphine antinociception (Fig. 8B). These results indicate that vlPAG glutamatergic output to the LC is crucial for systemic morphine antinociception but may work in tandem with other descending structures (e.g., the RVM) to achieve the full morphine effect.

We next sought to determine whether RVM→LC inhibitory projections shape nociception. We first challenged RVM$^{Vgat\text{-}cre}$::hM4Di mice with systemic CNO to determine the effect of inhibiting all RVM inhibitory neurons. This global inhibition had no effect on baseline nociception or morphine (5 mg/kg, s.c.) antinociception on the hot plate (fig. S7). In contrast, suppression of RVM inhibitory output to the LC via local CNO infusion increased hot plate withdrawal

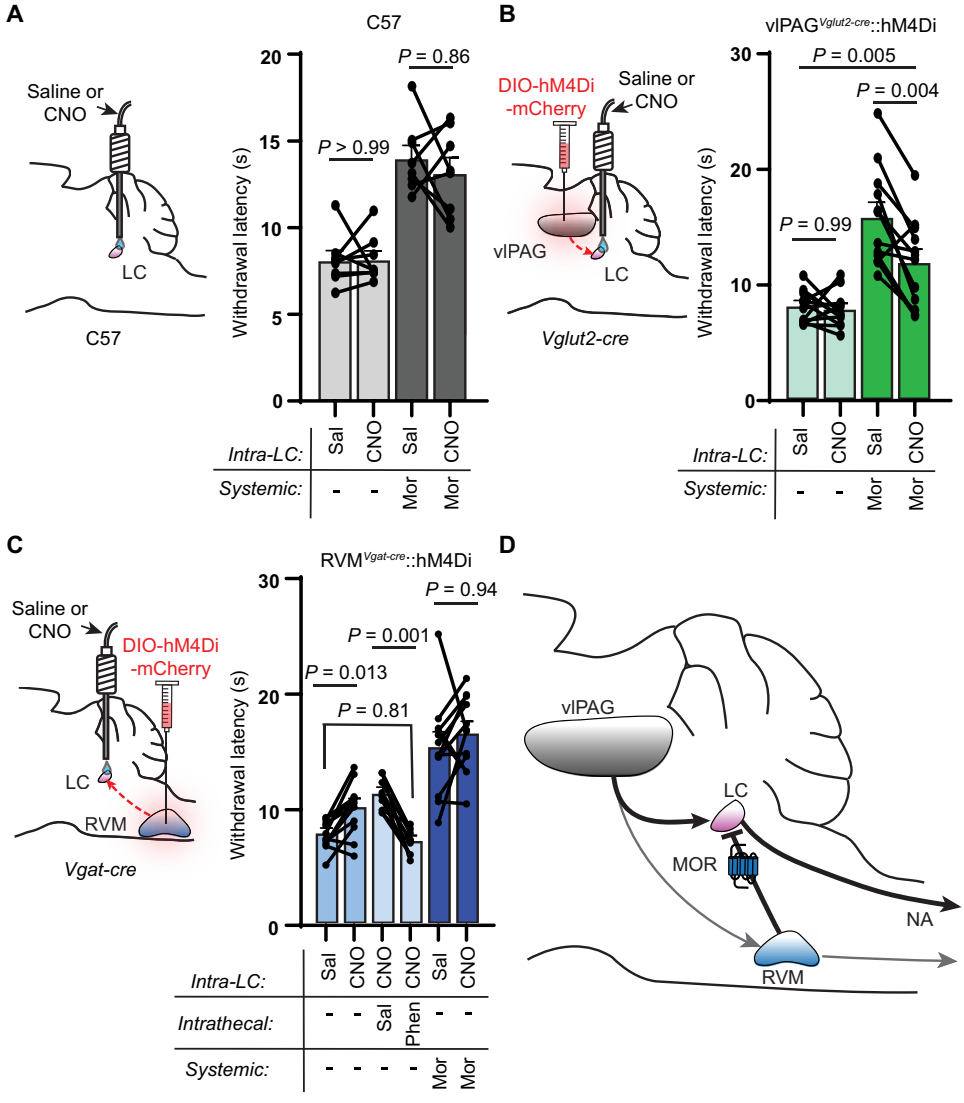

Fig. 8. Pathway-specific modulation of vlPAG and RVM terminals in the LC modulates nociceptive behavior. (**A**) Left: Bilateral cannula placement over the LC in uninjected control mice. Right: Hot plate withdrawal latencies of control mice microinfused in the LC with saline (150 nl) versus CNO (3 μM, 150 nl) without (light gray) and with morphine (5 mg/kg s.c.) (dark gray; two-way repeated-measures ANOVA with Tukey's multiple comparisons test; $n = 8$ mice; saline versus CNO effect, $P = 0.4178$, $F_{1,7} = 0.7412$). (**B**) Left: Bilateral viral injection of AAV-DIO-hM4Di-mCherry in the vlPAG of *Vglut2-cre* mice with bilateral cannula placement over the LC. Right: Hot plate withdrawal latencies after microinfusion with saline versus CNO without (light green) and with morphine (5 mg/kg s.c.) (dark green; two-way repeated-measures ANOVA with Sidak's multiple comparisons test; $n = 12$ mice; saline versus CNO effect, $P = 0.0022$, $F_{1,11} = 15.72$). (**C**) Left: Bilateral viral injection of AAV-DIO-hM4Di-mCherry in the RVM of *Vgat-cre* mice with bilateral cannula placement over the LC. Right: Hot plate withdrawal latencies after microinfusion of saline versus CNO (blue bars, $n = 12$ mice), microinfusion of CNO with intrathecal injections of saline versus phentolamine (5 μg, light blue bars, $n = 9$ mice), and microinfusion of saline versus CNO with morphine (5 mg/kg s.c.) (dark blue, $n = 12$ mice; mixed-effects analysis with matching across row and Tukey's multiple comparisons test, $P < 0.0001$, $F_{2.560,25.09} = 27.36$). (**D**) Circuit diagram of DPMS inputs to the LC and their opioid sensitivity. Data in each graph reported as means ± SEM.

latencies, which is consistent with disinhibition of descending LC-NA neurons (Fig. 8C). Confirming this hypothesis, intrathecal phentolamine completely blocked the resulting antinociception. In contrast, chemogenetic suppression of this pathway had no effect on morphine antinociception, which is consistent with occlusion of MOR-mediated synaptic suppression by hM4Di activation (and vice versa). Together, these pathway-specific manipulations are consistent with direct excitation of LC by vlPAG glutamatergic neurons and tonic inhibition by RVM inhibitory neurons that leads to opioid-driven disinhibition in the presence of opioids to shape nociceptive behavior (Fig. 8D).

DISCUSSION

In this study, we establish a critical and previously underappreciated role for LC activity in systemic morphine antinociception and delineate synaptic mechanisms by which the vlPAG and RVM activate the LC in response to supraspinal opioid signaling. Although the LC is frequently included in DPMS circuit models, previous lesion studies aimed at identifying the sources of spinal NA concluded that the LC makes only a minor contribution, which led to a focus on the A7 nucleus (*29*, *52*, *53*, *79*, *80*). In contrast, our results establish a central role for the LC in morphine antinociception in mice. We find that systemic morphine induces c-Fos in LC-NA neurons, consistent with neuronal activation, although other morphine-responsive receptors, such as G_s-coupled Mas-related G protein–coupled receptors (*81*–*83*), could be involved. However, we also observed morphine activation of the LC in real time using fiber photometry. Furthermore, c-Fos induction was attenuated by opioid antagonism, pointing to a role for upstream opioid receptors in the vlPAG and/or the inhibitory RVM→LC pathway uncovered in this study. Apparent discrepancies between our findings and previous work might be attributed to differences in the anatomy and/or neurochemistry of the DPMS in rats and mice. In our hands, mouse LC neurons exhibited a comparatively small opioid response, whereas the rat LC is profoundly inhibited by opioids (*42*, *43*). In either case, because transgenic mice are widely used in contemporary pain research, understanding their descending pain modulatory circuitry is of great importance.

The vlPAG has been long appreciated to contribute to morphine antinociception due to the initial finding that local vlPAG opioid administration produces potent antinociception. However, its role has not been unequivocally established, as lesion studies in rats arrive at different conclusions (*84*, *85*), perhaps due to differences in lesion protocol and the limited precision of this method. Using cell type–specific chemogenetic loss of function, our work demonstrates that glutamatergic output from the vlPAG is critical for morphine antinociception. This is consistent with classic models of opioid-mediated disinhibition of vlPAG neurons that project to the RVM, which we found to send prominent axon collaterals to the LC. This unexpected finding suggests that activation of antinociceptive projections neurons in the vlPAG recruits the LC and RVM in parallel. This model is further bolstered by the relatively low mu opioid sensitivity of vlPAG excitatory synaptic transmission onto LC neurons such that disinhibited vlPAG output should faithfully drive LC activity in the presence of systemic MOR agonists.

Our results also reveal several distinctions between the role of NA in spinal and supraspinal opioid antinociception. At low doses of morphine (e.g., 5 mg/kg), the antinociception is mediated primarily by supraspinal opioid receptors, as evidenced by nearly complete loss of systemic morphine antinociception upon chemogenetic vlPAG silencing and loss of descending NA. In contrast, higher morphine doses (>10 mg/kg) may directly engage spinal opioid receptors, as intrathecal phentolamine only partially blocks the resulting antinociception. These results are consistent with a proposed multiplicative effect of supraspinal and spinal opioids at lower morphine doses, whereas the effect of either site can mediate antinociception at higher doses (*41*, *86*, *87*). However, within the spinal cord, NA-opioid interactions are likely critical. In our data, both $vlPAG^{Vglut2\text{-}cre}$::hM3Dq and low-dose systemic morphine antinociception were completely blocked by spinal phentolamine or naltrexone. Since both involve the vlPAG, one possibility is that spinal endogenous opioids are recruited via the RVM. Alternatively, because the antinociception produced by intrathecal NA is blocked by intrathecal opioid antagonists (*88*), NA may drive endogenous opioid release in the spinal cord. However, neither spinal NA nor spinal opioids alone are sufficient to support the vlPAG-driven antinociception. Intrathecal naltrexone blocked systemic morphine antinociception at all doses tested, consistent with spinal opioid signaling being a critical end point. Because intrathecal morphine antinociception does not require spinal NA signaling, we posit that spinal opioid receptors gate spinal NA–mediated antinociception.

Our results indicate a major role for the LC, as well as the glutamatergic vlPAG projections to it, in systemic morphine antinociception. However, upon inhibition of either, abrogation of antinociception was incomplete. This suggests that other parallel descending pathways also contribute to systemic morphine effects. A likely possibility is that vlPAG projections to the RVM contribute to morphine antinociception in a parallel and additive fashion, taking advantage of vlPAG bifurcations to both structures. Alternatively, A5 and A7 are other sources of descending NA that may be involved in morphine antinociception. A large body of literature supports an antinociceptive function for A7 that depends on spinal NA signaling (*22*, *51*–*53*). More recently, A5 has been proposed to mediate diffuse noxious inhibitory control of pain downstream of the LC (*89*, *90*). Both of these regions also receive anatomical inputs from the vlPAG and the RVM (*30*, *35*). Future experiments are required to assess the contributions of these pathways to systemic opioid antinociception.

Our unexpected finding that vlPAG projections are biased toward dorsal LC raises questions about how the vlPAG contributes to LC-mediated behaviors. In our study, slice electrophysiology recordings were made from ventral LC-NA neurons to bias our physiological interrogation of the circuit toward putative descending LC neurons that modulate pain. However, the vlPAG most certainly provides excitation to dorsal, ascending LC neurons as well. In line with this, a recent study of lateral PAG inputs to the LC reported excitatory postsynaptic responses in most LC neurons, without regard to subregion (*33*). It has been hypothesized that each module might be separately recruited via distinct synaptic inputs in the context of different behavioral states, which, at least in the context of pain modulation, would help reconcile their opposing pain facilitatory and pain inhibitory actions (*18*, *19*). Although subpopulations of glutamatergic vlPAG neurons that distinctly target dorsal and ventral LC neurons may exist, they were not distinguished in our experiments. It is possible that the dorsal and ventral LC modules might differentially respond to salient and noxious sensory stimuli such that the early and late phases of the Ca^{2+} response observed in the Hargreaves test (Fig. 7B) might be mediated by different

populations of neurons. Alternatively, parallel activation of ascending and descending LC-NA neurons could support the complex nocifensive behaviors that occur in response to a noxious stimulus. In this case, noxious stimulus–driven vlPAG activity might simultaneously activate the ventral LC to dampen nociception, and the dorsal LC to promote arousal and the formation of memories to facilitate noxious stimulus avoidance in the future (*91*–*93*). Similarly, LC activity has been shown to be crucial for the expression of stress-induced anxiety (*94*). In this way, sustained, parallel recruitment of ascending and descending LC modules in response to injury, while battling ongoing pain hypersensitivity, could contribute to the comorbid anxiety associated with chronic pain (*95*–*97*). In relation, how these circuits might be dysregulated in the face of injury to support pain hypersensitivity and chronic pain, and how they might contribute to opioid tolerance, remains to be established.

Last, our discovery of a largely inhibitory drive from the RVM to the ventral LC was unexpected. While chemogenetic inhibition of these RVM outputs specifically to the LC caused spinal NA–dependent antinociception, presumably via disinhibition of the LC, inhibiting all RVM inhibitory neurons had no effect on either opioid-naïve nociception or morphine antinociception (fig. S7). This may be due to interactions between pro- and antinociceptive RVM projections to the spinal cord (*2*, *98*). LC-projecting RVM neurons do not appear to project to the spinal cord and instead send ascending projections to the thalamus, making it currently unclear how LC-projecting RVM neurons might fit into the canonical On- and Off-cell framework. Our Ca^{2+} measurements from RVM inhibitory terminals in the LC showed an increase in activity in response to noxious stimuli, which closely follows the time course of vlPAG→LC neuronal activity such that these two opposing inputs might be driven by the same ascending pathway. As our anatomical results suggest that these neurons do not receive direct input from the vlPAG, how RVM→LC neurons are activated by noxious sensory stimuli remains to be determined. If vlPAG neurons do control RVM→LC neuron activity, it likely occurs locally within the RVM microcircuit. Although we have established that silencing inhibitory RVM→LC neurons is antinociceptive, future studies are required to understand how this MOR-sensitive input contributes to descending pain modulation in various contexts.

Overall, this work establishes the LC as a central source of spinal NA that generates systemic morphine antinociception and identifies excitatory input from vlPAG neurons as the critical synapse that drives LC in this context. In addition, it establishes a synaptic pathway between the medial RVM and LC that can produce acute antinociception via disinhibition of LC-NA neurons, leading to spinal NA release. Although this study used an exogenous opioid drug, the circuit elements uncovered are likely also involved in other forms of top-down descending pain modulation that rely on endogenous opioids, such as placebo- and stress-induced analgesia.

MATERIALS AND METHODS

Animals

All procedures were performed in accordance with protocols approved by the University of California, San Diego Institutional Animal Care and Use Committee (UCSD IACUC protocol S16171) and guidelines from the U.S. National Institutes of Health *Guide for Care and Use of Laboratory Animals*. Mice were group-housed, maintained on a 12-hour reversed light/dark cycle, and allowed ad libitum access to food and water. Experiments were performed under red lighting during the dark period. Strains used include the following: C57Bl/6J (The Jackson Laboratory, stock no. 664), *Dbh-cre* [MMRRC/GENSAT, no. 032081-UCD, Tg(DBH-cre)HK212Gsat/Mmucd], *Slc17a6-IRES-cre* [*Vglut2-cre*, The Jackson Laboratory, stock no. 028863, B6J.129S6(FVB)-Slc17a6$^{tm2(cre)Lowl}$/MwarJ], and *Slc32a1-IRES-cre* [*Vgat-IRES-cre*, The Jackson Laboratory, stock no. 028862, B6J.129S6(FVB)-Slc32a1$^{tm2(cre)Lowl}$/MwarJ]. *Ai14* tdTomato [The Jackson Laboratory, stock no. 7914, B6.Cg-Gt(ROSA)$^{26Sortm14(CAG-tdTomato)Hze}$/J] and *Oprm1*$^{fl/fl}$ (The Jackson Laboratory, stock no. 30074, B6;129-Oprm1$^{tm1.1Cgrf}$/KffJ) mice were also obtained from The Jackson Laboratory but bred in-house to *Dbh-cre* mice. Mice were used for experiments between the ages of 8 to 20 weeks. Both male and female mice were used for all experiments.

Drugs

The following drugs were purchased from HelloBio: CNO (HB1807), NBQX disodium salt (HB0443), TTX citrate (HB1035), GABAzine (SR 95531 hydrobromide; HB0901), and (R)-CPP (HB0021). Naltrexone hydrochloride (N3136), naloxone hydrochloride (N7758), 4-AP (A78403), and strychnine hydrochloride (S8753) were purchased from Sigma-Aldrich. Morphine sulfate was purchased from Spectrum Chemicals (M1167). Phentolamine hydrochloride was purchased from Abcam (ab120791). DAMGO was purchased from R&D Systems Inc. (1171). CNV-Y-DAMGO was prepared in house, as previously reported (*48*). CNV-NA was synthesized in-house based on the protocol of Robinson *et al.* (*99*). Drugs to be injected or intracranially infused were dissolved in 0.9% saline and sterile-filtered before use.

Viral constructs

The following viruses were purchased from Addgene: AAV8-hsyn-DIO-hM4Di-mCherry (Addgene 44362, titer 2.3×10^{13}), AAV8-hsyn-DIO-hM3Dq-mCherry (Addgene 44361, titer 2.1×10^{13}), AAVretro-hsyn-cre (Addgene 105553, titer 2.1×10^{13}), AAVretro-Ef1a-FlpO (Addgene 55637, titer 1.3×10^{13}), AAV1-syn-FLEX-jGCaMP8s (Addgene 162377, titer 2.3×10^{13}), AAV8-Ef1a-Con/Fon-GCaMP6m (Addgene 137119, titer 2.4×10^{13}), AAVretro-Ef1a-DIO-FlpO (Addgene 87306, titer 1.6×10^{13}), and AAVretro-hSyn-DIO-EGFP (Addgene 50457, titer 1.4×10^{13}). The following were made and titered in-house using Addgene plasmids: AAVDJ-hsyn-DIO-mCherry (Addgene 50459, titer 3.5×10^{12}), AAVDJ-ef1a-fDIO-EYFP (Addgene 55641, titer 2×10^{11}), AAVDJ-Ef1a-mCherry-IRES-cre (Addgene 55632, titer 4.3×10^{12}), and AAVDJ-ef1a-DIO-ChR2(H134R)-mCherry (Addgene 20297, titer 2.55×10^{13}). AAV1-FLEX-ef1a-taCasp3-TEVP (titer 2.1×10^{12}) and AAV1-CAG-FLEX-tdTomato (titer 7.6×10^{12}) were both purchased from the UNC Vector Core. scAAV1-hSyn-cre (titer 2.8×10^{13}) was purchased from WZBiosciences. We received AAVDJ-CAG-DIO-Kir2.1-P2A-zsGreen and AAVDJ-Ef1a-DIO-Synaptophysin-eGFP as a gift from the laboratory of B. Lim.

Intrathecal injections

Intrathecal injections were performed according to the protocol detailed by Hylden and Wilcox (*100*). Acute percutaneous intrathecal injections were executed using a 30-gauge 1-inch needle attached to a 10-μl Hamilton syringe via polyethylene tubing. Mice were lightly anesthetized with 2% isoflurane, the fur over their lumbar spine was removed with electric clippers, and the skin was disinfected with

alternating povidone iodine solution and isopropyl alcohol. While firmly holding the pelvic girdle, the needle was inserted into the skin over the lumbar spine at a 20° angle. The needle was guided between the vertebrae until it entered the spinal column, which was signified by a tail flick. Each intrathecal injection was given at a volume of 5 μl. Mice were given at least 10 to 15 min to recover from the intrathecal injection before behavioral testing.

Behavior assays

Thermal nociceptive behavior

Mice were habituated to a hot plate (Thermo Fisher Scientific, no. SP88857100) at room temperature in a clear plastic cylinder for at least 20 s. During testing, mice were placed on the hot plate at 52°C and observed for a nocifensive response (hind paw withdrawal, shaking, licking, or jumping). Mice were immediately removed from the hot plate at the first sign of a nocifensive response, and the time to paw withdrawal was recorded. Each trial was terminated after a maximum of 60 s, even if no withdrawal occurred, to avoid tissue damage. Mice were tested twice on the hot plate during each session with a 3- to 5-min intertrial interval.

For fiber photometry recordings, mice were tested on the Hargraves apparatus (IITC Life Science, Model 400 Heated Base, Series 8 Model 390G light source). Mice were placed on the heated surface (32°C) in a clear plastic cylinder and habituated for 15 min. During testing, the Hargreaves apparatus was set to either 10 or 50% intensity. The light stimulus was targeted to one hind paw at a time and was manually removed when a withdrawal response was observed. Each trial was automatically terminated at 20 s if no withdrawal response was observed. Mice were tested three times on each paw with a 3- to 5-min intertrial interval. The response to the different intensities was tested on different days.

To test response to a cold thermal stimulus, the acetone drop assay was used. Mice were placed in a clear cylinder on an elevated wire grid and allowed to habituate for 15 min. A syringe fitted with polyethylene tubing (Braintree Scientific Inc.) was used to place a single drop of acetone or room temperature water on the plantar surface of one hind paw at a time. The mice were tested with each solution on different days. Within a recording day, each hind paw was tested twice, with a 3- to 5-min intertrial interval.

Mechanical nociceptive behavior

Mice were tested for mechanical thresholds using either the von Frey or pin prick assay. In both cases, mice were placed in a clear cylinder on an elevated wire grid and allowed to habituate for 20 min. Using the up-down method (*101*), von Frey filaments (Ugo Basile) of varying stiffnesses were applied to each hind paw separately, with a 3-min break until returning to the first paw, until a withdrawal response could be recorded and a 50% withdrawal threshold could be calculated. The resulting threshold values (in grams) for each paw were averaged together to calculate the mechanical threshold for each mouse. During the pin prick assay, a fine insect pin (size 000, Thermo Fisher Scientific, NC9295307) was applied to the plantar surface of each hind paw five times at 5-min intervals for a total of 10 trials. Response to pin was calculated as the number out of 10 trials in which the mouse displayed nocifensive withdrawal behavior.

For fiber photometry experiments, mice were probed for mechanical responses using either a pin prick or nonnoxious von Frey fiber. Mice were placed in a clear cylinder on an elevated wire grid and allowed to habituate for 15 min. The plantar surface of each hind paw was probed with either a 0.16-g von Frey fiber (Ugo Basile) or fine insect pin (size 000, Thermo Fisher Scientific, NC9295307). Each hind paw was probed three times with each stimulus during a single testing session with a 1- to 3-min intertrial interval.

Elevated plus maze and open field

Mice were placed on an elevated plus maze with two open and two closed arms (52-cm diameter) and video-recorded (Logitech) for a 20-min period. The SMARTv3.0 video tracking software (Panlab) was used to measure the percent of time spent in the open versus closed arms of the apparatus. In addition, the distance traveled during the 20-min testing period was reported. Similarly, locomotion in the open field was tested by placing mice in a square arena (18 cm by 18 cm) for a 20-min testing period and the SMARTv3.0 software was used to track mouse trajectory and calculate distance traveled.

Surgeries

Before surgery, mice were deeply anesthetized by induction at 5% isoflurane, after which anesthesia was maintained by 2% isoflurane (SomnoSuite, Kent Scientific). After mice were placed in a stereotaxic frame (David Kopf Instruments), a midline incision was made through the scalp following fur removal and site preparation by alternating povidone iodine and 70% isopropyl alcohol. The virus (100 to 250 nl) was injected at a rate of 100 nl/min at defined stereotaxic coordinates. The stereotaxic coordinates used for viral injections are as follows: vlPAG: angle ±10°, anterior-posterior (AP) −4.60 mm, medial-lateral (ML) ±0.32 mm, and DV 2.85 mm; RVM: angle 10°, AP −7.00 mm, ML +0.26 and −0.67 mm, and DV 6.30 and 6.26 mm; LC: angle ±10°, AP −5.45, ML ±0.75 mm, and DV 4.10 mm. For bilateral LC cannula implants, the following coordinates were used: angle ±15°, AP −5.45 mm, ML ±0.9 mm, and DV 3.80 mm. Guide cannulas were 26-gauge, included a 5-mm pedestal, and were cut 5 mm below the pedestal. Internal cannulas were 33-gauge and included 1-mm projection from the end of the guide cannula (Plastics One/Protech International Inc.). Cannulas were secured to the surface of the skull using light-cured dental epoxy and anchored by one screw. Optical fibers for fiber photometry (200 μm, 0.37 NA, Neurophotometrics) were secured in the same fashion using the following coordinates: vlPAG: angle −10°, AP −4.60 mm, ML ±0.35 mm, and DV 2.60 mm; LC: angle −15°, AP −5.45, ML ±0.90 mm, and DV 3.90 mm. For all surgeries, mice were administered ketoprofen (5 mg/kg, MWI Veterinary Supply) before the end of surgery and 24 hours later and monitored for recovery for 5 days. Mice were given at least 1 week to recover from cannula or optical implant surgeries before behavior or fiber photometry recordings.

Brain slice preparation

Mice were anesthetized with isoflurane before rapid decapitation. Brains were removed, blocked, and mounted in a VT1000s vibratome (Leica Instruments). Coronal midbrain slices (190 μm) containing the LC were prepared in ice-cold choline-based artificial cerebrospinal fluid (ACSF) containing 25 mM $NaHCO_3$, 1.25 mM NaH_2PO_4, 2.5 mM KCl, 7 mM $MgCl_2$, 25 mM glucose, 0.5 mM $CaCl_2$, 110 mM choline chloride, 11.6 mM ascorbic acid, and 3.1 mM pyruvic acid, equilibrated with 95% O_2/5% CO_2. Slice were transferred to 32°C oxygenated ACSF containing 125 mM NaCl, 2.5 mM KCl, 25 mM $NaHCO_3$, 1.25 mM NaH_2PO_4, 2 mM $CaCl_2$, 1 mM $MgCl_2$, and 10 mM glucose, osmolarity 290. Slices were

incubated for 20 min and then brought to room temperature before recording.

Slice electrophysiology

Slice physiology experiments were performed in a chamber continuously perfused with warmed (32°C) ACSF equilibrated with 95% O_2/5% CO_2. Recording pipettes were pulled from borosilicate glass on a P-1000 Flaming/Brown micropipette puller (Sutter Instruments) to a resistance of 1 to 3.5 megohms. Recordings were made with an Axopatch 700B amplifier (Axon Instruments), and data were sampled at 10 kHz, filtered at 3 kHz, and acquired using National Instruments acquisition boards and a custom version of ScanImage written in MATLAB (MathWorks). LC neurons were visually identified and confirmed to exhibit tonic action potential spiking of ~1.5 Hz. Recordings were biased toward the ventral portion of LC on each coronal slice. Recordings of action potential spiking were made in current clamp with patch pipettes filled with an internal solution containing 135 mM $KMeSO_3$, 5 mM KCl, 5 mM Hepes, 4 mM Mg–adenosine triphosphate (MgATP), 0.3 mM Na–guanosine triphosphate (NaGTP), 10 mM phosphocreatine, and 1.1 mM EGTA (pH 7.25, 290 mOsm kg^{-1}). Firing rate versus current input (*f-I*) curves were constructed using 1-s steps of direct current input (−100, 50, 100, 150, 200, 250, and 300 pA) 10 s apart. The effect of CNV-Y-DAMGO circulating in the bath on spiking was determined by presenting a single 50-ms flash of ultraviolet (UV) light [365-nm light-emitting diode (LED), 84 mW, pE-300ultra, CoolLED] and recording tonic spiking for 20 s before and 100 s after the flash. Firing rate in the 10 s before and after the flash, latency to spike after the flash as a measure of the pause in action potential firing, and the change in membrane potential after the flash were measured. For the effect of optogenetically mediated excitation of inputs to LC on tonic spiking, 50 × 2-ms pulses of blue light (470 nm, 18 mW, pE-300ultra LED) at 25 Hz for a total of 2 s were delivered. The firing rate in the 2 s before and 2 s during blue light stimulation were used to compare light-evoked excitation or inhibition.

Recordings of evoked postsynaptic currents were made in voltage clamp with patch pipettes filled with an internal solution containing 135 mM $CsMeSO_3$, 3.3 mM QX314 Cl^- salt, 10 mM Hepes, 4 mM MgATP, 0.3 mM NaGTP, 8 mM phosphocreatine, and 1 mM EGTA (pH 7.2 to 7.3, 295 mOsm kg^{-1}) for optogenetically evoked postsynaptic currents and the K^+-based internal solution from above when measuring opioid- or NA-evoked currents. Cells were rejected if holding currents became more negative than −200 pA or if series resistance exceeded 25 megohms. Recordings of opioid-evoked and NA-evoked currents were conducted at a holding potential of −55 mV and recorded in the presence of NBQX (10 μM), CPP (10 μM), GABAzine (20 μM), and strychnine (10 μM) to eliminate synaptic currents. As in current clamp, CNV-Y-DAMGO was photoactivated by a single 50-ms flash of UV light. Caged NA was circulated at 10 μM and photoreleased using a 500-ms full-field UV light flash (365 nm LED, 84 mW, pE-300ultra, CoolLED). While recording oEPSCs and oIPSCs in LC neurons, ChR2 terminals were stimulated with a single 5-ms flash of blue light. Initial characterization of oEPSCs and oIPSCs was done in the absence of synaptic blockers, and each current was isolated by holding the LC neuron at −70 or 0 mV, respectively. Further pharmacological verification of evoked currents was performed with AMPA blocker NBQX (10 μM), NMDA blocker CPP (10 μM), GABA-A receptor blocker GABAzine (SR 95531, 20 μM), glycine receptor blocker strychnine (10 μM), sodium channel blocker TTX (1 μM), and potassium channel blocker 4-AP (100 μM). Opioid sensitivity of evoked postsynaptic currents was assessed by bath perfusion of mu-opioid receptor agonist DAMGO (1 μM). All electrophysiology data were processed in Igor Pro (Wavemetrics).

Fiber photometry

For fiber photometry recordings in LC, *Dbh-cre* mice were injected in LC with DIO-GCaMP8s + mCherry and implanted unilaterally in the right LC. For recordings from PAG→LC neurons, *Vglut2-cre* mice were injected in unilateral right LC with AAVretro-FlpO and in unilateral right PAG with Cre-on/Flp-on-GCaMP6M with implants in unilateral right PAG. For recordings of RVM inhibitory terminals in LC, *Vgat-cre* mice were injected in bilateral RVM with DIO-GCaMP8s and implanted unilaterally in the right LC. For fiber photometry recordings, a commercially available fiber photometry system was used (FP3001, Neurophotometrics). Recordings were made through a single-fiber optic cable. For LC recordings, a 470-nm LED was used to record GCaMP activity and 560-nm LED for control wavelength. For PAG→LC and RVM terminal recordings, a 470-nm LED was used to record GCaMP activity and 415-nm LED isosbestic wavelength was used as control. Data analysis of fluorescence recordings was conducted using the pMAT open source photometry analysis package (*102*) in MATLAB 2021a (MathWorks), which allows for the scaling of the control channel to correct for movement and bleaching, and subsequently calculates peri-event time histograms of $\Delta F/F$ and *z*-score values. Other calculations, such as baseline correction and area under the curve analysis, were completed using custom scripts in Igor Pro (Wavemetrics). Fluorescence traces are presented in the figures as means ± SEM of multiple individual traces from all mice (e.g., for recordings from 10 mice with 4 trials each, the figures reflect means ± SEM of 40 trials).

Fluorescent in situ hybridization

FISH was performed either in naïve wild-type mice or in mice bilaterally injected in RVM with green retrobeads (Lumafluor Inc.). Mice were deeply anesthetized and decapitated. Brains were quickly removed and frozen in Tissue-Tek OCT medium (Sakura) on dry ice until completely solid. Brain slices (8 μm) were prepared on a cryostat (Leica CM 1950) and adhered to SuperFrost Plus slides (VWR). Samples were fixed with 4% paraformaldehyde and processed according to instructions in the ACD Bio RNAscope Fluorescent Multiplex Assay (Fluorescent Reagent Kit v2) manual and coverslipped with ProLong antifade media (Molecular Probes). Images were taken on a Keyence microscope (BZ-X710) using a 60× 1.4 numerical aperture oil immersion objective configured for structured illumination microscopy. Puncta counting in FISH images was completed using a custom pipeline designed in CellProfiler.

Histology

For all other mice, brains were fixed using chilled 4% paraformaldehyde in phosphate-buffered saline (PBS) by transcardial perfusion and cryoprotected in 30% sucrose in PBS solution. In some cases, spinal cords were also removed and processed in the same fashion. Brain slices (40 μm) or spinal sections (100 μm) were prepared on a freezing microtome (Thermo Fisher Scientific, Microm HM450). For sections selected for immunohistochemistry, slices were blocked in PBS-Triton (0.3% Triton X-100 in 1× PBS) with 5% donkey or goat serum for 1 hour at room temperature. Incubation in primary

antibodies occurred in PBS-Triton plus 1% serum at 4°C for 24 to 72 hours. Following three 10-min wash steps in PBS, the slices were incubated in PBS-Triton plus 1% serum with secondary antibodies for 4 hours at room temperature. After three more wash steps, slices were mounted and coverslipped with mounting media containing 4′,6-diamidino-2-phenylindole (DAPI) (Vector Laboratories, H1200). Primary antibodies (1:500) used include rabbit anti–c-Fos (9F6) (no. 2250, Cell Signaling Technology), rabbit anti-TH (AB152, EMD Millipore), and mouse anti-TH (T2928, Sigma-Aldrich). Secondary antibodies used include Alexa Fluor 488 donkey anti-rabbit, Alexa Fluor 555 donkey anti-mouse, Alexa Fluor 488 goat anti-rabbit, and Alexa Fluor 555 goat anti-rabbit (1:500, Invitrogen). After mounting, slices were imaged on a Keyence microscope (BZ-X710) at ×2, ×10, or ×20 magnification. Cell counts and quantification of fluorescent colocalization were performed using custom pipelines in Cell Profiler. Pixel intensity analysis was performed in ImageJ, z scores were calculated in Microsoft Excel, and resulting values were graphed in GraphPad Prism.

Statistics

Data in each figure are presented as means ± SEM, and individual data points from experimental replicates are plotted in most cases. Statistical analyses were performed in GraphPad Prism. The test performed, number of experimental replicates, statistics provided by analysis of variance (ANOVA) and two-way ANOVA tests, and P values for the overall test are provided in the figure legend. Individual P values resulting from post hoc tests to correct for multiple comparisons appear in the figures. Repeated measures within individual replicates were taken into account where applicable based on experimental design. Data were tested for normality using the Shapiro Wilk test, and nonparametric statistics were used when necessary and possible. In certain cases, when multiple conditions included different numbers of experimental replicates, a mixed-effects model was used in place of a two-way ANOVA. Raw data for each graph as well as the results of statistical tests, including two-way ANOVA results for both variables and the interaction between them, are available in the data S1 spreadsheet.

Supplementary Materials

This PDF file includes:
Figs. S1 to S7
Legend for data S1

Other Supplementary Material for this manuscript includes the following:
Data S1

REFERENCES AND NOTES

1. M. J. Millan, Descending control of pain. *Prog. Neurobiol.* **66**, 355–474 (2002).
2. A. François, S. A. Low, E. I. Sypek, A. J. Christensen, C. Sotoudeh, K. T. Beier, C. Ramakrishnan, K. D. Ritola, R. Sharif-Naeini, K. Deisseroth, S. L. Delp, R. C. Malenka, L. Luo, A. W. Hantman, G. Scherrer, A brainstem-spinal cord inhibitory circuit for mechanical pain modulation by GABA and Enkephalins. *Neuron* **93**, 822–839.e6 (2017).
3. A. Basbaum, H. L. Fields, Endogenous pain control systems: Brainstem spinal pathways and endorphin circuitry. *Annu. Rev. Neurosci.* **7**, 309–338 (1984).
4. M. M. Heinricher, I. Tavares, J. L. Leith, B. M. Lumb, Descending control of nociception: Specificity, recruitment and plasticity. *Brain Res. Rev.* **60**, 214–225 (2009).
5. B. K. Lau, C. W. Vaughan, Descending modulation of pain: The GABA disinhibition hypothesis of analgesia. *Curr. Opin. Neurobiol.* **29**, 159–164 (2014).
6. H. L. Fields, J. Bry, I. Hentall, G. Zorman, The activity of neurons in the rostral medulla of the rat during withdrawal from noxious heat. *J. Neurosci.* **3**, 2545–2552 (1983).
7. M. M. Heinricher, Z. F. Cheng, H. L. Fields, Evidence for two classes of nociceptive modulating neurons in the periaqueductal gray. *J. Neurosci.* **7**, 271–278 (1987).
8. M. M. Heinricher, M. M. Morgan, V. Tortorici, H. L. Fields, Disinhibition of off-cells and antinociception produced by an opioid action within the rostral ventromedial medulla. *Neuroscience* **63**, 279–288 (1994).
9. L. D. Aimone, S. L. Jones, G. F. Gebhart, Stimulation-produced descending inhibition from the periaqueductal gray and nucleus raphe magnus in the rat: Mediation by spinal monoamines but not opioids. *Pain* **31**, 123–136 (1987).
10. T. S. Jensen, T. L. Yaksh, Spinal monoamine and opiate systems partly mediate the antinociceptive effects produced by glutamate at brainstem sites. *Brain Res.* **321**, 287–297 (1984).
11. D. L. Hammond, T. L. Yaksh, Antagonism of stimulation-produced antinociception by intrathecal administration of methysergide or phentolamine. *Brain Res.* **298**, 329–337 (1984).
12. T. L. Yaksh, Direct evidence that spinal serotonin and noradrenaline terminals mediate the spinal antinociceptive effects of morphine in the periaqueductal gray. *Brain Res.* **160**, 180–185 (1979).
13. H. K. Proudfit, D. L. Hammond, Alterations in nociceptive threshold and morphine-induced analgesia produced by intrathecally administered amine antagonists. *Brain Res.* **218**, 393–399 (1981).
14. D. Budai, I. Harasawa, H. L. Fields, Midbrain periaqueductal gray (PAG) inhibits nociceptive inputs to sacral dorsal horn nociceptive neurons through α_2-adrenergic receptors. *J. Neurophysiol.* **80**, 2244–2254 (1998).
15. R. P. Ganley, M. M. de Sousa, K. Werder, T. Öztürk, R. Mendes, M. Ranucci, H. Wildner, H. U. Zeilhofer, Targeted anatomical and functional identification of antinociceptive and pronociceptive serotonergic neurons that project to the spinal dorsal horn. *eLife* **12**, e78689 (2023).
16. R. Suzuki, W. Rahman, S. P. Hunt, A. H. Dickenson, Descending facilitatory control of mechanically evoked responses is enhanced in deep dorsal horn neurones following peripheral nerve injury. *Brain Res.* **1019**, 68–76 (2004).
17. C. I. Svensson, T. K. Tran, B. Fitzsimmons, T. L. Yaksh, X.-Y. Hua, Descending serotonergic facilitation of spinal ERK activation and pain behavior. *FEBS Lett.* **580**, 6629–6634 (2006).
18. S. Hirschberg, Y. Li, A. Randall, E. J. Kremer, A. E. Pickering, Functional dichotomy in spinal- vs prefrontal-projecting locus coeruleus modules splits descending noradrenergic analgesia from ascending aversion and anxiety in rats. *eLife* **6**, e29808 (2017).
19. Y. Li, L. Hickey, R. Perrins, E. Werlen, A. A. Patel, S. Hirschberg, M. W. Jones, S. Salinas, E. J. Kremer, A. E. Pickering, Retrograde optogenetic characterization of the pontospinal module of the locus coeruleus with a canine adenoviral vector. *Brain Res.* **1641**, 274–290 (2016).
20. A. Burnett, G. F. Gebhart, Characterization of descending modulation of nociception from the A5 cell group. *Brain Res.* **546**, 271–281 (1991).
21. F. M. Clark, D. C. Yeomans, H. K. Proudfit, The noradrenergic innervation of the spinal cord: Differences between two substrains of Sprague-Dawley rats determined using retrograde tracers combined with immunocytochemistry. *Neurosci. Lett.* **125**, 155–158 (1991).
22. F. M. Clark, H. K. Proudfit, The projection of noradrenergic neurons in the A7 catecholamine cell group to the spinal cord in the rat demonstrated by anterograde tracing combined with immunocytochemistry. *Brain Res.* **547**, 279–288 (1991).
23. F. M. Clark, H. K. Proudfit, The projection of locus coeruleus neurons to the spinal cord in the rat determined by anterograde tracing combined with immunocytochemistry. *Brain Res.* **538**, 231–245 (1991).
24. F. M. Clark, H. K. Proudfit, The projections of noradrenergic neurons in the A5 catecholamine cell group to the spinal cord in the rat: Anatomical evidence that A5 neurons modulate nociception. *Brain Res.* **616**, 200–210 (1993).
25. K. N. Westlund, R. M. Bowker, M. G. Ziegler, J. D. Coulter, Noradrenergic projections to the spinal cord of the rat. *Brain Res.* **263**, 15–31 (1983).
26. W. L. West, D. C. Yeomans, H. K. Proudfit, The function of noradrenergic neurons in mediating antinociception induced by electrical stimulation of the locus coeruleus in two different sources of Sprague-Dawley rats. *Brain Res.* **626**, 127–135 (1993).
27. L. Hickey, Y. Li, S. J. Fyson, T. C. Watson, R. Perrins, J. Hewinson, A. G. Teschemacher, H. Furue, B. M. Lumb, A. E. Pickering, Optoactivation of locus ceruleus neurons evokes bidirectional changes in thermal nociception in rats. *J. Neurosci.* **34**, 4148–4160 (2014).
28. M. Sasa, K. Munekiyo, Y. Osumi, S. Takaori, Attenuation of morphine analgesia in rats with lesions of the locus coeruleus and dorsal raphe nucleus. *Eur. J. Pharmacol.* **42**, 53–62 (1977).
29. D. L. Hammond, H. K. Proudfit, Effects of locus coeruleus lesions on morphine-induced antinociception. *Brain Res.* **188**, 79–91 (1980).
30. D. Bajic, H. K. Proudfit, Projections of neurons in the periaqueductal gray to pontine and medullary catecholamine cell groups involved in the modulation of nociception. *J. Comp. Neurol.* **405**, 359–379 (1999).
31. L. A. Schwarz, K. Miyamichi, X. J. Gao, K. T. Beier, B. Weissbourd, K. E. Deloach, J. Ren, S. Ibanes, R. C. Malenka, E. J. Kremer, L. Luo, Viral-genetic tracing of the input-output organization of a central noradrenaline circuit. *Nature* **524**, 88–92 (2015).
32. J.-H. Kim, G. Gangadharan, J. Byun, E.-J. Choi, C. J. Lee, H.-S. Shin, Yin-and-yang bifurcation of opioidergic circuits for descending analgesia at the midbrain of the mouse. *Proc. Natl. Acad. Sci. U.S.A.* **115**, 11078–11083 (2018).

33. K. Barcomb, S. S. Olah, M. J. Kennedy, C. P. Ford, Properties and modulation of excitatory inputs to the locus coeruleus. *J. Physiol.* **600**, 4897–4916 (2022).
34. M. Ennis, M. Behbehani, M. T. Shipley, E. J. van Bockstaele, G. Aston-Jones, Projections from the periaqueductal gray to the rostromedial pericoerulear region and nucleus locus coeruleus: Anatomic and physiologic studies. *J. Comp. Neurol.* **306**, 480–494 (1991).
35. F. M. Clark, H. K. Proudfit, Projections of neurons in the ventromedial medulla to pontine catecholamine cell groups involved in the modulation of nociception. *Brain Res.* **540**, 105–115 (1991).
36. M. Ennis, G. Aston-Jones, Activation of locus coeruleus from nucleus paragigantocellularis: A new excitatory amino acid pathway in brain. *J. Neurosci.* **8**, 3644–3657 (1988).
37. M. Ennis, G. Aston-Jones, R. Shiekhattar, Activation of locus coeruleus neurons by nucleus paragigantocellularis or noxious sensory stimulation is mediated by intracoerulear excitatory amino acid neurotransmission. *Brain Res.* **598**, 185–195 (1992).
38. X. Gu, Y. Z. Zhang, J. J. O'Malley, C. C. De Preter, M. Penzo, M. A. Hoon, Neurons in the caudal ventrolateral medulla mediate descending pain control. *Nat. Neurosci.* **26**, 594–605 (2023).
39. T. L. Yaksh, T. A. Rudy, Narcotic analgestics: CNS sites and mechanisms of action as revealed by intracerebral injection techniques. *Pain* **4**, 299–359 (1978).
40. D. Budai, H. L. Fields, Endogenous opioid peptides acting at μ-opioid receptors in the dorsal horn contribute to midbrain modulation of spinal nociceptive neurons. *J. Neurophysiol.* **79**, 677–687 (1998).
41. T. L. Yaksh, T. A. Rudy, Studies on the direct spinal action of narcotics in the production of analgesia in the rat. *J. Pharmacol. Exp. Ther.* **202**, 411–428 (1977).
42. J. T. Williams, T. M. Egan, R. A. North, Enkephalin opens potassium channels on mammalian central neurones. *Nature* **299**, 74–77 (1982).
43. M. R. Banghart, B. L. Sabatini, Photoactivatable neuropeptides for spatiotemporally precise delivery of opioids in neural tissue. *Neuron* **73**, 249–259 (2012).
44. A. T. Luskin, L. Li, X. Fu, K. Barcomb, T. Blackburn, E. M. Li, A. Rana, R. C. Simon, L. Sun, A. D. Murry, S. A. Golden, G. D. Stuber, C. P. Ford, L. Gu, M. R. Bruchas, A diverse network of pericoerulear neurons control arousal states. bioRxiv 2022.06.30.498327 [Preprint] (2022). https://doi.org/10.1101/2022.06.30.498327.
45. T. Shoda, K. Fukuda, H. Uga, H. Mima, H. Morikawa, Activation of μ-Opioid receptor induces expression of c-*fos* and *junB* via mitogen-activated protein kinase cascade. *Anesthesiology* **95**, 983–989 (2001).
46. R. Weibel, D. Reiss, L. Karchewski, O. Gardon, A. Matifas, D. Filliol, J. A. J. Becker, J. N. Wood, B. L. Kieffer, C. Gaveriaux-Ruff, Mu opioid receptors on primary afferent Nav1.8 neurons contribute to opiate-induced analgesia: Insight from conditional knockout mice. *PLOS ONE* **8**, e74706 (2013).
47. Y. Zhang, M. Rózsa, Y. Liang, D. Bushey, Z. Wei, J. Zheng, D. Reep, G. J. Broussard, A. Tsang, G. Tsegaye, S. Narayan, C. J. Obara, J. X. Lim, R. Patel, R. Zhang, M. B. Ahrens, G. C. Turner, S. S. H. Wang, W. L. Korff, E. R. Schreiter, K. Svoboda, J. P. Hasseman, I. Kolb, L. L. Looger, Fast and sensitive GCaMP calcium indicators for imaging neural populations. *Nature* **615**, 884–891 (2023).
48. X. Ma, D. A. Johnson, X. J. He, A. E. Layden, S. P. McClain, J. C. Yung, A. Rizzo, J. Bonaventura, M. R. Banghart, In vivo photopharmacology with a caged mu opioid receptor agonist drives rapid changes in behavior. *Nat. Methods* **20**, 682–685 (2023).
49. X. J. He, J. Patel, C. E. Weiss, X. Ma, B. L. Bloodgood, M. R. Banghart, Convergent, functionally independent signaling by mu and delta opioid receptors in hippocampal parvalbumin interneurons. *eLife* **10**, e69746 (2021).
50. M. Torrecilla, C. L. Marker, S. C. Cintora, M. Stoffel, J. T. Williams, K. Wickman, G-protein-gated potassium channels containing Kir3.2 and Kir3.3 subunits mediate the acute inhibitory effects of opioids on locus ceruleus neurons. *J. Neurosci.* **22**, 4328–4334 (2002).
51. D. C. Yeomans, H. K. Proudfit, Antinociception induced by microinjection of substance p into the A7 catecholamine cell group in the rat. *Neuroscience* **49**, 681–691 (1992).
52. D. C. Yeomans, F. M. Clark, J. A. Paice, H. K. Proudfit, Antinociception induced by electrical stimulation of spinally projecting noradrenergic neurons in the A7 catecholamine cell group of the rat. *Pain* **48**, 449–461 (1992).
53. J. E. Holden, E. J. Schwartz, H. K. Proudfit, Microinjection of morphine in the A7 catecholamine cell group produces opposing effects on nociception that are mediated by α1- and α2- adrenoceptors. *Neuroscience* **91**, 979–990 (1999).
54. P. Tovote, M. S. Esposito, P. Botta, F. Chaudun, J. P. Fadok, M. Markovic, S. B. E. Wolff, C. Ramakrishnan, L. Fenno, K. Deisseroth, C. Herry, S. Arber, A. Lüthi, Midbrain circuits for defensive behaviour. *Nature* **534**, 206–212 (2016).
55. V. K. Samineni, J. G. Grajales-Reyes, B. A. Copits, D. E. O'Brien, S. L. Trigg, A. M. Gomez, M. R. Bruchas, R. W. Gereau, Divergent modulation of nociception by glutamatergic and GABAergic neuronal subpopulations in the periaqueductal gray. *eNeuro* **4**, ENEURO.0129-16.2017 (2017).
56. B. L. Roth, DREADDs for neuroscientists. *Neuron* **89**, 683–694 (2016).
57. M. M. Morgan, M. S. Gold, J. C. Liebeskind, C. Stein, Periaqueductal gray stimulation produces a spinally mediated, opioid antinociception for the inflamed hindpaw of the rat. *Brain Res.* **545**, 17–23 (1991).
58. F. A. Chaudhry, R. J. Reimer, E. E. Bellocchio, N. C. Danbolt, K. K. Osen, R. H. Edwards, J. Storm-Mathisen, The vesicular GABA transporter, VGAT, localizes to synaptic vesicles in sets of glycinergic as well as GABAergic neurons. *J. Neurosci.* **18**, 9733–9750 (1998).
59. G. Paxinos, K. B. J. Franklin, *The Mouse Brain in Stereotaxic Coordinates*, *2nd Edition* (Academic Press, 2001).
60. X. H. Hou, M. Hyun, J. Taranda, K. W. Huang, E. Todd, D. Feng, E. Atwater, D. Croney, M. L. Zeidel, P. Osten, B. L. Sabatini, Central control circuit for context-dependent micturition. *Cell* **167**, 73–86.e12 (2016).
61. G. Aston-Jones, M. T. Shipley, G. Chouvet, M. Ennis, E. van Bockstaele, V. Pieribone, R. Shiekhattar, H. Akaoka, G. Drolet, B. Astier, P. Charléty, R. J. Valentino, J. T. Williams, Afferent regulation of locus coeruleus neurons: Anatomy, physiology and pharmacology. *Prog. Brain Res.* **88**, 47–75 (1991).
62. C.-C. Kuo, J.-C. Hsieh, H.-C. Tsai, Y.-S. Kuo, H.-J. Yau, C.-C. Chen, R.-F. Chen, H.-W. Yang, M.-Y. Min, Inhibitory interneurons regulate phasic activity of noradrenergic neurons in the mouse locus coeruleus and functional implications. *J. Physiol.* **598**, 4003–4029 (2020).
63. G. Aston-Jones, Y. Zhu, J. P. Card, Numerous GABAergic afferents to locus ceruleus in the pericerulear dendritic zone: Possible interneuronal pool. *J. Neurosci.* **24**, 2313–2321 (2004).
64. E. E. Bagley, S. L. Ingram, Endogenous opioid peptides in the descending pain modulatory circuit. *Neuropharmacology* **173**, 108131 (2020).
65. D. B. Reichling, A. I. Basbaum, Contribution of brainstem GABAergic circuitry to descending antinociceptive controls: I. GABA-immunoreactive projection neurons in the periaqueductal gray and nucleus raphe magnus. *J. Comp. Neurol.* **302**, 370–377 (1990).
66. M. M. Morgan, K. L. Whittier, D. M. Hegarty, S. A. Aicher, Periaqueductal gray neurons project to spinally projecting GABAergic neurons in the rostral ventromedial medulla. *Pain* **140**, 376–386 (2008).
67. C. Park, J.-H. Kim, B.-E. Yoon, E.-J. Choi, C. J. Lee, H.-S. Shin, T-type channels control the opioidergic descending analgesia at the low threshold-spiking GABAergic neurons in the periaqueductal gray. *Proc. Natl. Acad. Sci. U.S.A.* **107**, 14857–14862 (2010).
68. B. A. Vogt, P. R. Hof, D. P. Friedman, R. W. Sikes, L. J. Vogt, Norepinephrinergic afferents and cytology of the macaque monkey midline, mediodorsal, and intralaminar thalamic nuclei. *Brain Struct. Funct.* **212**, 465–479 (2008).
69. B. Zingg, B. Peng, J. Huang, H. W. Tao, L. I. Zhang, Synaptic specificity and application of anterograde transsynaptic AAV for probing neural circuitry. *J. Neurosci.* **40**, 3250–3267 (2020).
70. B. Zingg, X. Chou, Z. Zhang, L. Mesik, F. Liang, H. W. Tao, L. I. Zhang, AAV-mediated anterograde transsynaptic tagging: Mapping corticocollicular input-defined neural pathways for defense behaviors. *Neuron* **93**, 33–47 (2017).
71. T. M. Egan, G. Henderson, R. A. North, J. T. Williams, Noradrenaline-mediated synaptic inhibition in rat locus coeruleus neurones. *J. Physiol.* **345**, 477–488 (1983).
72. G. Aston-Jones, F. E. Bloom, Norepinephrine-containing locus coeruleus neurons in behaving rats exhibit pronounced responses to non-noxious environmental stimuli. *J. Neurosci.* **1**, 887–900 (1981).
73. S. J. Sara, M. Segal, Plasticity of sensory responses of locus coeruleus neurons in the behaving rat: Implications for cognition. *Prog. Brain Res.* **88**, 571–585 (1991).
74. S. J. Sara, The locus coeruleus and noradrenergic modulation of cognition. *Nat. Rev. Neurosci.* **10**, 211–223 (2009).
75. E. M. Vazey, D. E. Moorman, G. Aston-Jones, Phasic locus coeruleus activity regulates cortical encoding of salience information. *Proc. Natl. Acad. Sci. U.S.A.* **115**, E9439–E9448 (2018).
76. L. E. Fenno, C. Ramakrishnan, Y. S. Kim, K. E. Evans, M. Lo, S. Vesuna, M. Inoue, K. Y. M. Cheung, E. Yuen, N. Pichamoorthy, A. S. O. Hong, K. Deisseroth, Comprehensive dual- and triple-feature intersectional single-vector delivery of diverse functional payloads to cells of behaving mammals. *Neuron* **107**, 836–853.e11 (2020).
77. T. W. Chen, T. J. Wardill, Y. Sun, S. R. Pulver, S. L. Renninger, A. Baohan, E. R. Schreiter, R. A. Kerr, M. B. Orger, V. Jayaraman, L. L. Looger, K. Svoboda, D. S. Kim, Ultrasensitive fluorescent proteins for imaging neuronal activity. *Nature* **499**, 295–300 (2013).
78. T. J. Stachniak, A. Ghosh, S. M. Sternson, Chemogenetic synaptic silencing of neural circuits localizes a hypothalamus→midbrain pathway for feeding behavior. *Neuron* **82**, 797–808 (2014).
79. J. F. Miller, H. K. Proudfit, Antagonism of stimulation-produced antinociception from ventrolateral pontine sites by intrathecal administration of α-adrenergic antagonists and naloxone. *Brain Res.* **530**, 20–34 (1990).
80. K. Nuseir, H. K. Proudfit, Bidirectional modulation of nociception by GABA neurons in the dorsolateral pontine tegmentum that tonically inhibit spinally projecting noradrenergic A7 neurons. *Neuroscience* **96**, 773–783 (2000).
81. T. L. Yaksh, K. A. Eddinger, S. Kokubu, Z. Wang, A. DiNardo, R. Ramachandran, Y. Zhu, Y. He, F. Weren, D. Quang, S. A. Malkmus, K. Lansu, W. K. Kroeze, B. Eliceiri, J. J. Steinauer, P. W. Schiller, P. Gmeiner, L. M. Page, K. R. Hildebrand, Mast cell degranulation and fibroblast activation in the morphine-induced spinal mass. *Anesthesiology* **131**, 132–147 (2019).
82. J. Hami, V. von Bohlen Und Halbach, A. Tetzner, T. Walther, O. von Bohlen Und Halbach, Localization and expression of the Mas-related G-protein coupled receptor member D (MrgD) in the mouse brain. *Heliyon* **7**, e08440 (2021).

83. Z. Hu, T. Zhao, T. Chen, D. Wang, Chronic activation of Mas-related gene receptors (Mrg) reduces the potency of morphine-induced analgesia via PKC pathway in naive rats. *Brain Res.* **1722**, 146363 (2019).
84. J. C. Yeung, T. L. Yaksh, T. A. Rudy, Effects of brain lesions on the antinociceptive properties of morphine in rats. *Clin. Exp. Pharmacol. Physiol.* **2**, 261–268 (1975).
85. J. O. Dostrovsky, J. F. W. Deakin, Periaqueductal grey lesions reduce morphine analgesia in the rat. *Neurosci. Lett.* **4**, 99–103 (1977).
86. J. C. Yeung, T. A. Rudy, Sites of antinociceptive action of systemically injected morphine: Involvement of supraspinal loci as revealed by intracerebroventricular injection of naloxone. *J. Pharmacol. Exp. Ther.* **215**, 626–632 (1980).
87. J. C. Yeung, T. A. Rudy, Multiplicative interaction between narcotic agonisms expressed at spinal and supraspinal sites of antinociceptive action as revealed by concurrent intrathecal and intracerebroventricular injections of morphine. *J. Pharmacol. Exp. Ther.* **215**, 633–642 (1980).
88. S. W. Yang, Z. H. Zhang, R. Wang, Y. F. Xie, J. T. Qiao, N. Dafny, Norepinephrine and serotonin-induced antinociception are blocked by naloxone with different dosages. *Brain Res. Bull.* **35**, 113–117 (1994).
89. M. W. Kucharczyk, F. Di Domenico, K. Bannister, A critical brainstem relay for mediation of diffuse noxious inhibitory controls. *Brain* **146**, 2259–2267 (2023).
90. M. W. Kucharczyk, F. Di Domenico, K. Bannister, Distinct brainstem to spinal cord noradrenergic pathways inversely regulate spinal neuronal activity. *Brain* **145**, 2293–2300 (2022).
91. G. R. Poe, S. Foote, O. Eschenko, J. P. Johansen, S. Bouret, G. Aston-Jones, C. W. Harley, D. Manahan-Vaughan, D. Weinshenker, R. Valentino, C. Berridge, D. J. Chandler, B. Waterhouse, S. J. Sara, Locus coeruleus: A new look at the blue spot. *Nat. Rev. Neurosci.* **21**, 644–659 (2020).
92. R. Jordan, G. B. Keller, The locus coeruleus broadcasts prediction errors across the cortex to promote sensorimotor plasticity. *eLife* **12**, RP85111 (2023).
93. A. Basu, J.-H. Yang, A. Yu, S. Glaeser-Khan, J. A. Rondeau, J. Feng, J. H. Krystal, Y. Li, A. P. Kaye, Frontal norepinephrine represents a threat prediction error under uncertainty. *Biol. Psychiatry*, (2024).
94. J. G. McCall, R. Al-Hasani, E. R. Siuda, D. Y. Hong, A. J. Norris, C. P. Ford, M. R. Bruchas, CRH engagement of the locus coeruleus noradrenergic system mediates stress-induced anxiety. *Neuron* **87**, 605–620 (2015).
95. M. H. Ossipov, K. Morimura, F. Porreca, Descending pain modulation and chronification of pain. *Curr. Opin. Support. Palliat. Care* **8**, 143–151 (2014).
96. M. Llorca-Torralba, G. Borges, F. Neto, J. A. Mico, E. Berrocoso, Noradrenergic locus coeruleus pathways in pain modulation. *Neuroscience* **338**, 93–113 (2016).
97. I. Suárez-Pereira, M. Llorca-Torralba, L. Bravo, C. Camarena-Delgado, C. Soriano-Mas, E. Berrocoso, The role of the Locus Coeruleus in pain and associated stress-related disorders. *Biol. Psychiatry* **91**, 786–797 (2022).
98. R. P. Ganley, M. M. de Sousa, M. Ranucci, K. Werder, T. Ozturk, H. Wildner, H. U. Zeilhofer, Descending GABAergic neurons of the RVM that mediate widespread bilateral antinociception. bioRxiv 2023.04.29.538824 [Preprint] (2023). https://doi.org/10.1101/2023.04.29.538824.
99. B. G. Robinson, J. R. Bunzow, J. B. Grimm, L. D. Lavis, J. T. Dudman, J. Brown, K. A. Neve, J. T. Williams, Desensitized D2 autoreceptors are resistant to trafficking. *Sci. Rep.* **7**, 4379 (2017).
100. J. L. K. Hylden, G. L. Wilcox, Intrathecal morphine in mice: A new technique. *Eur. J. Pharmacol.* **67**, 313–316 (1980).
101. S. R. Chaplan, F. W. Bach, J. W. Pogrel, J. M. Chung, T. L. Yaksh, Quantitative assessment of tactile allodynia in the rat paw. *J. Neurosci. Methods* **53**, 55–63 (1994).
102. C. A. Bruno, C. O'Brien, S. Bryant, J. I. Mejaes, D. J. Estrin, C. Pizzano, D. J. Barker, pMAT: An open-source software suite for the analysis of fiber photometry data. *Pharmacol. Biochem. Behav.* **201**, 173093 (2021).

Acknowledgments: We thank B. K. Lim for providing the Kir2.1 virus, A. E. Layden and J. Chang-Weinberg for genotyping support, and S. Han and W. Campana for helpful discussions. **Funding:** This work was supported by the Rita Allen Foundation, the Esther A. & Joseph Klingenstein Fund & Simons Foundation, the Brain & Behavior Research Foundation, the National Institute on Drug Abuse (R00DA034648 to M.R.B.), and the National Institute on Neurological Disorders and Stroke (RF1NS126073 to M.R.B.). **Author contributions:** Conceptualization: S.T.L., G.L., T.L.Y., and M.R.B. Formal analysis: S.T.L. and M.R.B. Funding acquisition: M.R.B. Investigation: S.T.L., J.P., and J.C.Y. Project administration: S.T.L. and M.R.B. Resources: S.A.B. and M.R.B. Supervision: S.T.L. and M.R.B. Visualization: S.T.L. and M.R.B. Writing—original draft: S.T.L. and M.R.B. Writing—review and editing: S.T.L., T.L.Y., and M.R.B. **Competing interests:** The authors declare that they have no competing interests. **Data and materials availability:** All data needed to evaluate the conclusions in the paper are present in the paper and/or the Supplementary Materials. Raw data, including complete statistics tables, are available in data S1 file. Correspondence and material requests should be addressed to M.R.B. (mbanghart@ucsd.edu).

Submitted 25 July 2023
Accepted 26 March 2024
Published 26 April 2024
10.1126/sciadv.adj9581

Science Advances
AAAS

Supplementary Materials for

Inputs to the locus coeruleus from the periaqueductal gray and rostroventral medulla shape opioid-mediated descending pain modulation

Susan T. Lubejko *et al.*

Corresponding author: Matthew R. Banghart, mbanghart@ucsd.edu

Sci. Adv. **10**, eadj9581 (2024)
DOI: 10.1126/sciadv.adj9581

The PDF file includes:

Other Supplementary Material for this manuscript includes the following:

Supplementary Figures

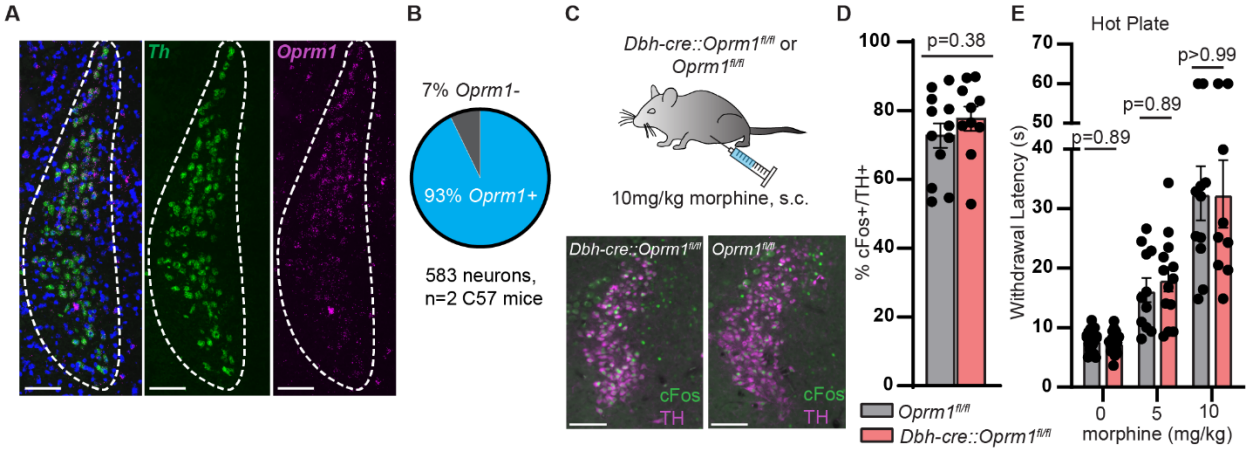

Figure S1. MORs in the LC are not responsible for morphine induced activity changes or behavior. **A.** Representative images of fluorescent *in situ* hybridization of the LC with probes against *Th* (green) and *Oprm1* (magenta). Scale bars 150 µm. **B.** Quantification of the percentage of *Th*+ LC neurons that express *Oprm1* transcripts. **C.** Top: morphine injections in *Dbh-cre::Oprm1*$^{fl/fl}$ mice and control *Oprm1*$^{fl/fl}$ littermates. Bottom: Representative images of morphine-induced c-Fos expression (green) and TH labeling (magenta). Scale bars 150 µm. **D.** Percentage of TH+ LC neurons that colocalize with green c-Fos signal (5-8 images analyzed per mouse; n=10 *Dbh-cre::Oprm1*$^{fl/fl}$, n=12 *Oprm1*$^{fl/fl}$; p=0.38, two-sided Mann-Whitney test). **E.** Hot plate withdrawal latencies at 0, 5, and 10 mg/kg morphine, *s.c.* (Mixed effects analysis with Sidak's multiple comparisons test; baseline n=18 *Dbh-cre::Oprm1*$^{fl/fl}$, n=18 *Oprm1*$^{fl/fl}$; 5 mg/kg morphine n=13 *Dbh-cre::Oprm1*$^{fl/fl}$, n=11 *Oprm1*$^{fl/fl}$; 10 mg/kg morphine n=9 *Dbh-cre::Oprm1*$^{fl/fl}$, n=11 *Oprm1*$^{fl/fl}$; genotype effect, p=0.835, F(1,34)=0.044).

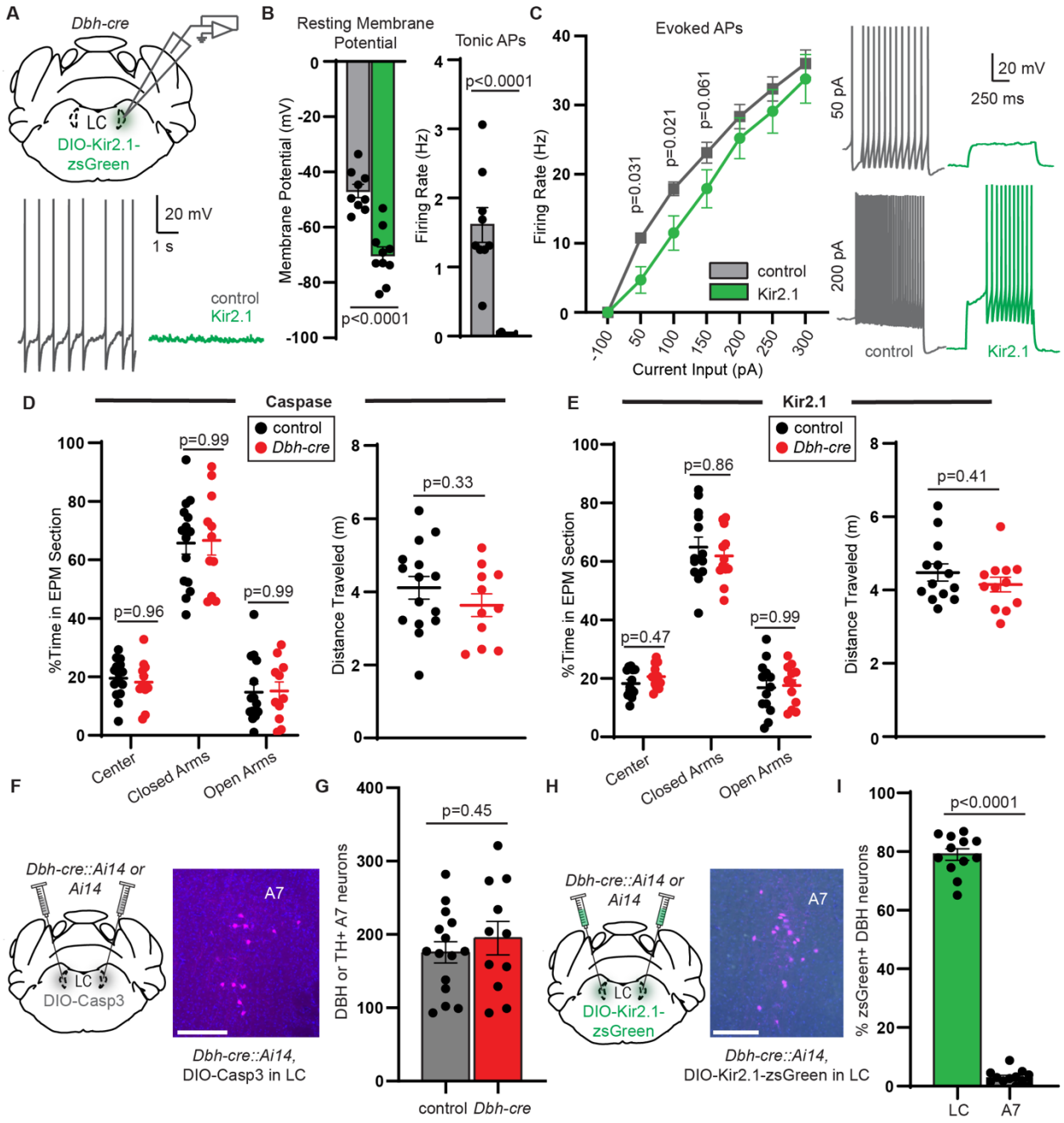

Figure S2. LC ablation or silencing does not affect baseline anxiety behavior or locomotion on the elevated plus maze or nucleus A7. A. Top, Slice electrophysiology recordings from Kir2.1-positive and -negative LC neurons. Bottom, representative traces of tonic firing in control vs. Kir2.1+ neurons. **B.** Resting membrane potential and tonic firing rate of control (n=9) vs. Kir2.1+ (n=10) neurons (two-sided Mann-Whitney tests). **C.** Left, f-I curves of control (n=9) vs. Kir2.1+ (n=10) neurons (two-sided Mann-Whitney test). Right, representative traces of evoked firing from a control (grey) and a Kir2.1+ (green) neuron at 50 pA (top) and 200 pA (bottom) current steps. **D.** Left: percentage of time spent in sections of the elevated plus maze (EPM) during a 20-minute session in *Dbh-cre* and control mice injected with AAV-DIO-Casp3 (same cohort from behavior in Figure 2; Two-way repeated measures ANOVA with Sidak's multiple comparisons test; n=11 *Dbh-cre* mice, n=15 control; p=0.489, F(1,24)=0.4934). Right: distance traveled during the 20-minute EPM session (two-sided Mann-Whitney test). **E.** Same as in D, but

for AAV-DIO-Kir2.1-zsGreen-injected mice from Figure 2. Left: Two-way repeated measures ANOVA with Sidak's multiple comparisons test; n=12 *Dbh-cre* mice, n=13 control; p=0.386, F(1,23)=0.7797. Right: two-sided Mann-Whitney test. **F.** Injection schematic of DIO-Casp3 in the LC and representative image of A7 tdTom expression from the same mice as in Figure 2L. **G.** Quantification of A7 neurons by genetic expression of tdTom in *Dbh-cre::Ai14* mice or immunohistochemical expression of TH in control mice (Two-sided unpaired t-test, t=0.7522; n=11 *Dbh-cre*, n=15 control). **H.** Same as F for DIO-Kir2.1-zsGreen injected mice from Figure 2N. **F, H.** Scale bars 150 μm. **I.** % of DBH+ LC and A7 neurons expressing zsGreen from 12 *Dbh-cre* mice. LC data reprinted directly from Fig. 2N (Two-sided paired t-test: t=34.29, n=12 pairs). Data presented as mean ± SEM.

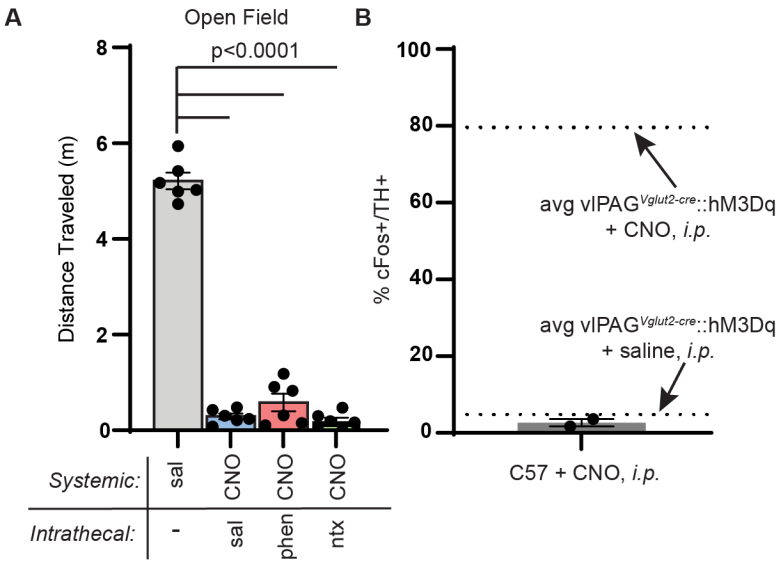

Figure S3. Chemogenetic vlPAG activation leads to decreased locomotion that can be decoupled from antinociception. A. Distance traveled (m) during a 30-minute open field session after systemic injection of saline or CNO (3 mg/kg, *i.p.*) with intrathecal saline, phentolamine (5 μg), or naltrexone (5 μg) in vlPAG$^{Vglut2\text{-}cre}$::hM3Dq mice (Repeated measures one-way ANOVA with Tukey's multiple comparisons test, $p<0.0001$, $F(2.467, 12.33)=392.1$). **B.** LC c-Fos expression induced by CNO injection in wild type mice expressed as % TH+ LC neurons that colocalize with c-Fos. Dashed lines represent the average c-Fos induction in the LC by CNO and saline in vlPAG$^{Vglut2\text{-}cre}$::hM3Dq mice in Figure 3E.

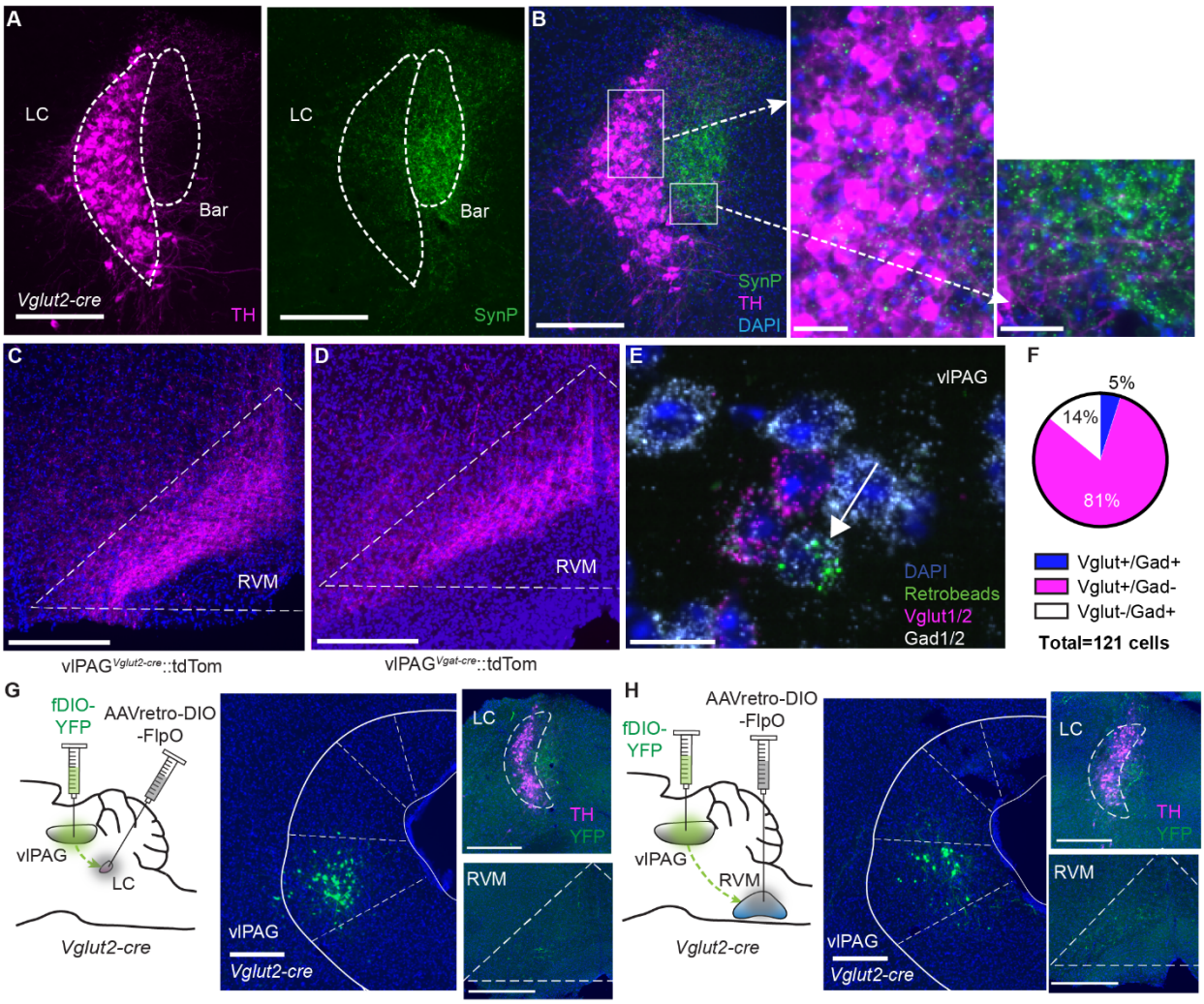

Figure S4. Characteristics of vlPAG output to the LC and RVM. A. Representative images of synaptophysin expression in the LC and peri-LC after DIO-synaptophysin-GFP injection in the vlPAG of a *Vglut2-cre* mouse. Bar, Barrington's nucleus (left: magenta TH IHC, right: green synaptophysin; scale bars 300 µm). **B.** Left: overlay of images in A. Right, example zoom in images of synaptophysin overlap with TH expression in the LC somatic region (left) and peri-LC (right). Left, Scale bar 300 µm. Center and right, scale bars 50 µm. **C.** Representative image of glutamatergic terminals (magenta) in the RVM of a *Vglut2-cre* mouse injected in the vlPAG with AAV-DIO-tdTom. Scale bar 300 µm. **D.** Representative image of GABAergic/glycinergic terminals in the RVM of a *Vgat-cre* mouse injected in the vlPAG with AAV-DIO-tdTom. Scale bar 300 µm. **E.** Representative image of retro-FISH depicting the vlPAG with colocalization of retrobeads from the RVM (green) and *Gad1/2* transcripts (white) within a single neuron, as well as nearby neurons expressing *Vglut1/2* transcripts (magenta). Scale bar 10 µm. **F.** Quantification of *Vglut1/2* and *Gad1/2* expression within retrobead-labeled vlPAG neurons. **G.** Left: viral injection to express YFP in vlPAG$^{Vglut2\text{-}cre}$→LC neurons. Center: YFP expression in the vlPAG. Right: YFP terminal expression in the LC/peri-LC (top) and RVM (bottom). **H.** Same as G for YFP expression in vlPAG$^{Vglut2\text{-}cre}$→RVM neurons. **G-H**. Scale bars 300 µm.

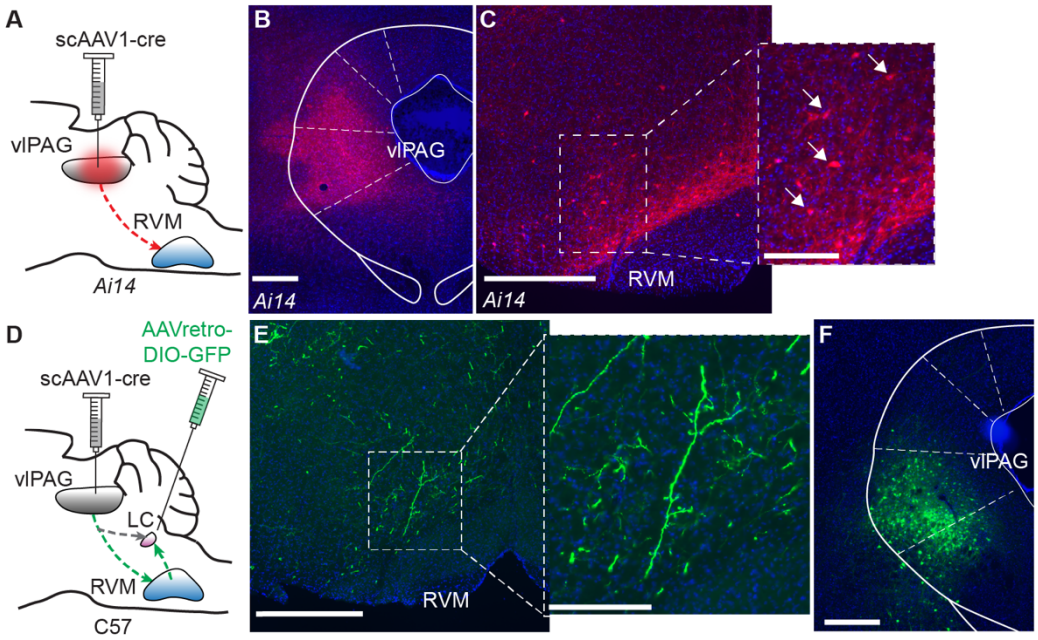

Figure S5. Anterograde viral methods used to interrogate a disynaptic vlPAG→RVM→LC circuit. **A.** Schematic of viral injections of scAAV1-cre in the vlPAG of *Ai14* mice. **B.** vlPAG injection site. Scale bar 300 μm. **C.** Resulting anterograde labeling in the RVM. Scale bar 300 μm. Inset: Zoomed in view. Arrows indicate anterogradely-labeled RVM cell bodies. Scale bar 100 μm. **D.** Viral injections used to capture RVM→LC neurons that receive input from the vlPAG. **E.** Representative image of resulting RVM labeling. Scale bar 300 μm. Inset: Zoomed in view reveals presence of GFP+ fibers in the RVM with no labeled cell bodies. Scale bar 100 μm. **F.** Labeling of vlPAG→LC neurons (grey arrow in D) by direct transduction of both viruses that is the putative source of the green terminals seen in E. Scale bar 300 μm.

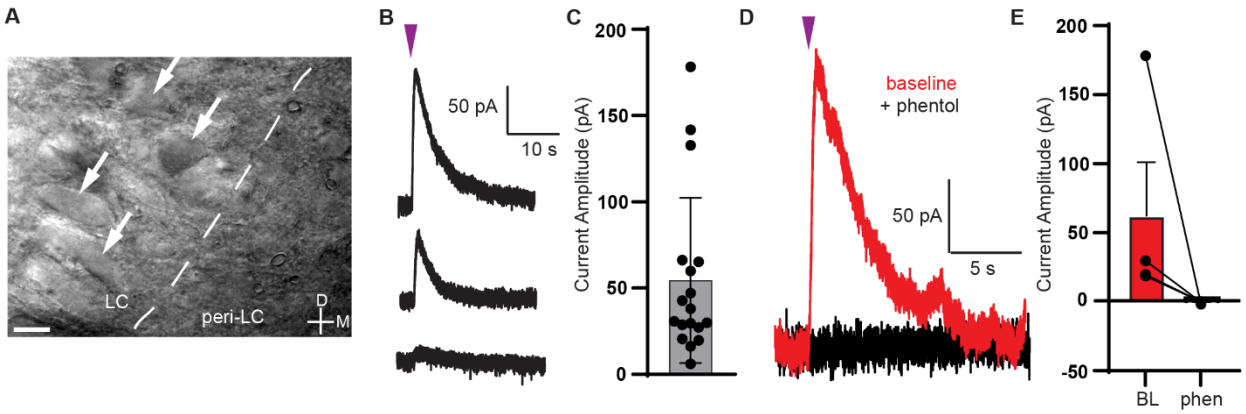

Figure S6. Confirmation of LC-NA neuron targeting by caged noradrenaline. A. Brightfield image (60x) of the border between the LC and peri-LC in an acute slice. White arrows indicate visually identified LC-NA neurons recorded in slice physiology experiments. Scale bar 20 µm. **B.** Example traces of large, average, and small current responses in LC neurons to a single 500-ms 365nm LED light flash (purple arrow) recorded in the presence of caged-NA (10 µM) and synaptic blockers. **C.** Peak current amplitudes (mean ± SD; n=18 neurons). 18/18 neurons exhibited a response greater than our threshold of 5 pA used to define a positive response. **D.** Example traces from a single LC neuron to a 500 ms UV LED flash before (red) and after (black) bath application of phentolamine. **E.** Current amplitudes before (BL) and after phentolamine from 4 LC neurons (mean ± SEM).

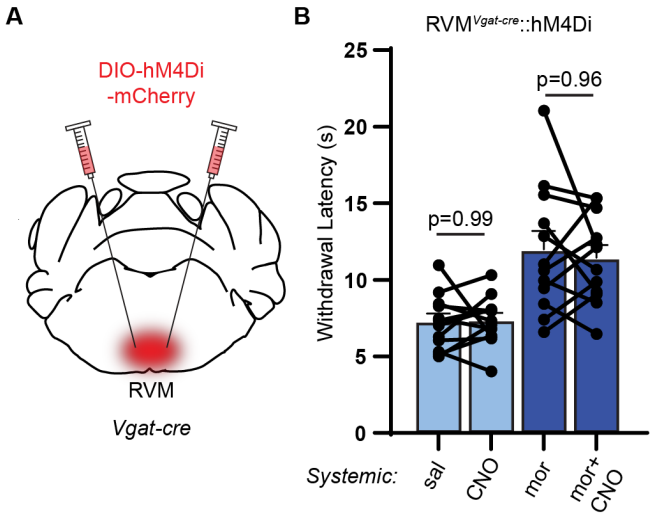

Figure S7. Inhibition of RVM GABAergic neurons does not affect baseline pain behavior or morphine antinociception. A. Bilateral viral injections of AAV-DIO-HM4Di-mCherry into the RVM of *Vgat-cre* mice. **B.** Hot plate withdrawal latencies of RVM$^{Vgat\text{-}cre}$::hM4Di mice administered 3 mg/kg CNO, *i.p.* vs. saline without (light blue) and with 5 mg/kg morphine, *s.c.* (dark blue bars, Two-way repeated measures ANOVA with Tukey's multiple comparisons test; n=12 mice; saline vs. CNO effect, p=0.725, F(1,11)=0.1307).

Supplemental Auxiliary Files

Data S1: source data for all figures